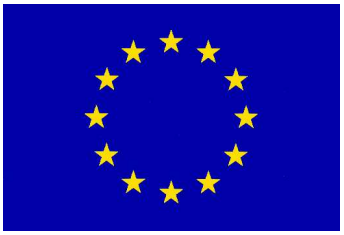

COMMISSION
OF THE EUROPEAN
COMMUNITIES

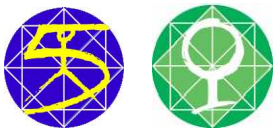

FP5 — EESD

CREST LEVEL ASSESSMENT OF
COASTAL STRUCTURES BY
FULL-SCALE MONITORING,
NEURAL NETWORK PREDICTION
AND HAZARD ANALYSIS
ON PERMISSABLE WAVE OVERTOPPING

CLASH

EVK3-CT-2001-00058

REPORT

Work package 5

Free Surface Numerical Modelling of Wave Interactions with Coastal Structures

DM Ingram, DM Causon, F Gao and CG Mingham
Centre for Mathematical Modelling and Flow Analysis, Manchester Metropolitan University

P Troch, T Li and J De Rouck
Department of Civil Engineering, Gent University

Abstract

The main objective of Workpackage 5 is to use numerical simulation of wave overtopping in order to solve the problem of suspected scale effects. A second, related, objective is to improve existing codes in such a way as they are able to simulate wave overtopping in a reliable way. The final, single, objective is to numerically model long waves on the shallow foreshore at Petten in order to understand the phenomenon of long waves and their effect on overtopping. This report deals with the work undertaken towards the first two objectives, the simulations undertaken for objective 3 are the subject of a separate report entitled "Influence of low-frequency waves on wave overtopping" by M.R.A. van Gent and C.C. Giarrusso and published by WL | Delft hydraulics in November 2003.

Realistic simulations of wave overtopping require numerical methods which are able accurately to simulate the shoaling, breaking and possible overturning of waves prior to their impact on the seawall. It is a further requirement that the simulation continues after impact, modelling the formation of the overtopping jet and the reflection of the wave. The research groups at Manchester Metropolitan University (MMU) and the University of Gent (UGent) have been working in parallel on the development of such numerical codes. The MMU code, AMAZON-SC, is a numerical wave flume based on the free surface capturing approach. While the UGent code, LVOF, is a numerical wave basin based on the volume of fluid approach. This report describes the progress of these numerical methods, in order to address the first two objectives of Workpackage 5. Their application to various cases, is also discussed, including: a test problem involving wave overtopping of a smooth sea-dike, wave overtopping at Samphire Hoe and an investigation of scale effects on rough impermeable structures.

The Report begins with a general introduction, followed by a section describing AMAZON-SC (the MMU code), a section describing LVOF (the UGent code) and then some general conclusions.

Contents

1 Background

Wave overtopping over a sea wall is a violently natural phenomenon that may affect the structural integrity of the sea defence. Once the highest run-up levels exceed the free board overtopping occurs and the associated instantaneous discharge over the wall may form a hazard to both the sea defence and its users. Waves breaking in the surf zone and elsewhere during overtopping processes are of particular interest because of the violent nature of the overtopping events associated with them. Indeed, breaking waves are the dominant feature in this complex flow field and vortex formation, turbulence and flow separation are associated with them. Thus the behaviour of the moving air-water interface (commonly referred to as the free surface) is of critical importance. The computational study of a viscous free surface flow under breaking waves is one of the most challenging topics, but the results, which may elucidate more detailed mechanisms, are both essential and desirable in both the research and engineering communities.

Generally, a relevant study involves the solution of moving boundary problems, where the effects of the free surface are distributed over a large proportion of the computational domain. Only the initial location and geometry of the free surface are known *a priori*. Since the location of the free surface is determined as part of the solution, gross topological changes that occur during the the processes of merging and breakup and which amplify wave-structure coupling problems must be handled. In particular, the presence of surface tension aggravates the situation and tends make things more difficult to model. A powerful numerical tool is required for handling arbitrarily shaped interfaces naturally. Many numerical approaches are available for studying flows of immiscible fluids with interfaces (e.g., the level set method [1, 2], the density function method [3], a front-tracking method [4], the smoothed particle hydrodynamics (SPH) method [5], the volume-of-fluid (VoF) method, a coupled level set and VoF method [6] and the free surface capturing approach [7]).

The development then of numerical methods capable of predicting solutions to flow problems with a moving free surface separating two segregated fluids are of fundamental interest in civil and coastal engineering. It is also clear that the movement of both the air and water are important in determining the flow physics and should therefore be fully accounted for in the solution. Traditional approaches to flow problems with free surfaces are surface-fitting methods and surface-tracking methods. Surface-fitting methods [8, 9] solve the flow equations in the liquid region only, and the free surface is treated as a moving boundary of the computational domain. This method is very efficient for simple free surface problems, but its applicability is limited by the skewness of the resulting computational grid. If the free surface becomes highly distorted such as in the case of wave breaking, a new grid may have to be generated to maintain the accuracy of the solution. The other obvious limitation of the method is that the effects of water-air interactions such as the trapping of an air bubble in a water ambient cannot be predicted, as in this case no explicit boundary conditions can be specified at the interface. The surface-tracking method, however, simulates both fluid regions on a fixed grid system, and the free surface is identified by a marker function such as the volume fraction in the widely used VoF method [10, 11, 12, 13, 14], such as using the modern PLIC (piecewise linear interface calculation) methods and purely Eulerian methods, respectively. For the former, without diffusion of the front, it is more promising than the original VoF method but at the cost of algorithmic complexity [15], especially in three-dimensional (3D) situations, where the tracking and reconstruction of free surfaces remains complicated and difficult in the context of mergers and breakups, as compared with purely Eulerian methods [16, 17, 13]. For the latter, in a new VoF solution currently developed by [18], the sharp interface is well maintained, while preserving the smoothness of the interface, especially no explicit expression for the interface reconstruction is required during tracking. As expected, it can be generalized well to 3D and used for several industrial applications. According to the current knowledge (Li, Ghent), the motions induced by breaking waves in a viscous numerical wave flume can be well captured using an advanced VoF method even

during a long time computation. This is because the intrinsic feature of VoF method is to identify the mass conservation and to directly handle the free surface, i.e., the shape of the free surface can be reconstructed from the distribution of the volume fraction function if necessary, indicating that one solves only its transport equation in the computations. In this way, the exact free- surface kinematic boundary condition and approximate free surface dynamic boundary condition are satisfied, which is similar to a moving mesh [18] [1] (also see the density function method [3]). As a consequence, this is a key point that the results obtained by Ghent's new solver look much more promising. Owing to the high quality in the stability with Ghent's new solver [19] even over a long period of integration time, on the other hand, this provides a great chance: the capture of the irregular waves, which is more challenging case, especially when waves break during overtopping of waves (see [19, 20]). In this method, a transport equation for the volume fraction function is solved at each time step and the shape of the free surface can then be reconstructed from the distribution of the volume fraction function. This method can define sharp interfaces and is robust, forming the basis of many VoF-type codes. The tracking and reconstruction of free surfaces, however, remains complicated and difficult, especially in three dimensions [17, 13].

More recently, another approach, referred to as the surface-capturing method, has been developed for free surface flows in closed containers [7] initially in the context of aerospace engineering. This method views the free surface as a contact discontinuity in the density field. Analogous to the shock-capturing method in compressible flow, the material interface is automatically captured as part of the evolving numerical solution, along with other flow variables such as pressure and velocity, by the enforcement of a conservation law. This eliminates the need for complex surface tracking and reconstruction procedures. The robustness and simplicity of the method modified appropriately for free surface flow problems is the basis of the MMU code, AMAZON-SC. AMAZON-SC utilises a time-accurate artificial compressibility method together with a high resolution Godunov-type scheme to replaces the pressure correction solver, used in a classical methods, providing much better resolution of the free surface.

One of the first tasks to be faced in Computational Fluid Dynamics (CFD) is the generation of a suitable computational computational mesh. Although a variety of mesh generation techniques are available [21], the generation of a suitable mesh for complex, multi-element, geometries is still a complex and tedious task. The two traditional approaches are: the use of a structured body-fitted mesh utilising a multi-block structure, in which the blocks may overlap, [22, 23, 24, 25] and the use of a completely unstructured body-fitted mesh [26, 27, 28]. Both of these approaches require significant effort to ensure that the generated mesh is of sufficient quality to both accurately represent the geometry and provide a high quality solution. Even in cases where a detailed description of the geometry is available from a CAD system, mesh generation can still be a complex task [29], requiring much more time to generate the grid than to simulate the fluid flow.

An alternative approach is the use of Cartesian cut cells. This conceptually simple approach "cuts" solid bodies out of a background Cartesian mesh. Although originally developed for potential flow, the method has been successfully applied to the Euler equations in two [30, 31, 32] and three [33, 34] space dimensions, to the Shallow Water Equations (SWE) [35] with static and moving boundaries and has been extended to deal with low speed incompressible flows [36, 37, 38] and flows involving moving material interfaces [39, 40, 41].

Under Workpackage 5 of the CLASH project a detailed study has been undertaken by researchers at both Manchester Metropolitan University (MMU) and the University of Gent (UGent) under which the capabilities of one existing (MMU) and one new (UGent) flow codes have been extended to attempt to provide general purpose tools which can be used to model individual overtopping events from the prototype sites at Zeebrugger, Ostia and

[1] Using a moving mesh, the boundary conditions at the interface are prescried on the actual location of the surface. No smearing of the interface is involved during tracking. As a result, a high order of accuracy can be preserved without the presence of breakwater.

Samphire Hoe on order to help asses the impact of scaling effects at these sites. UGent have developed a new numerical modelling for large eddy simulation (LES) of overtopping of water waves over sloping and vertical structures in a numerical wave tank. All the computed results shown in this report were produced with our recently developed solver, named LVoF, which has been published in JCP [19]. According to our suggestion, an additional job involves the extension to 3D problems. This content is also emphasized in this report. This is a VoF finite volume approach that incorporates the effects of surface tension. It has been verificated and validated by:

- the convergence history;
- the grid refinement effects;
- and the comparison with measurements available.

This follows the standard CFD procedure for testing a code. Also it is necessary in a certain test case (see [42]).

The surface capturing MMU code, AMAZON-SC [43, 44] which whilst already established for Cartesian cut cell grids has been extended to include both a porosity model and to solve the Navier-Stokes equations. This report describes the work undertaken at both institutions under Workpackage 5. Preliminary results on scaling effects for a model rough structure studied by MMU as input to Workpackage 7 are also presented.

2 MMU: AMAZON-SC

2.1 Cartesian cut cell methods

A Cartesian cut cell mesh is generated by "cutting" solid bodies out of a background Cartesian mesh. This results in the formation of fluid, solid and cut grid cells [32]. In order to generate the cut cells the body surfaces are represented using poly-lines, whose knots are defined in an anti-clockwise direction. Thus,

$$P_i = \{(x_0, y_0), \ldots, (x_j, y_j), \ldots, (x_n, y_n)\}$$

defines the i^{th} solid region.

The intersection points of a particular line segment, defined by its start and end coordinates (x_s, y_s) and (x_e, y_e), are found as follows. The address (I_s, J_s) of the cell containing the start coordinate is computed;

$$I_s = \text{int}\left(\frac{x_s - x_0}{\Delta x}\right) + 1 \text{ and } J_s = \text{int}\left(\frac{y_s - y_0}{\Delta y}\right) + 1 \tag{1}$$

where x_0 and y_0 are the coordinates of the bottom left corner of the computational domain. The address (I_e, J_e) of the end point is found in a similar way. For convenience we also identify which of the four quadrants $(0°, 90°]$, $(90°, 180°]$, $(180°, 270°]$ or $(270°, 360°]$ the slope of the line lies in.

The required intersection points can now be found. Figure 1 shows a line segment cutting a uniform background Cartesian mesh. Suppose that the intersection points of the line segment with cell (i, j) are to be found: clearly the point a at which the line segment enters the cell is already known because it is the exit point from the the previous cut cell. It thus remains necessary only to determine the exit point, b, for the cell (i, j). Since a is on the left side of the cell and $Q \in (0°, 90°]$ the exit point must lie above and to the right of a, locating the exit point on either the top or right hand side of the cell. The intersection points b, between the line segment and the line $y_{j+1} = y_0 + (j + 1)\Delta y$, and c, between the line segment and the line $x_{i+1} = x_0 + (i + 1)\Delta x$, are now found. Since $y_c > y_{j+1}$ the exit point must be (x_b, y_b). This process is repeated for all subsequent grid cells intersected

by the line segment until the cell (I_e, J_e) is reached. The cases where Q lies in the other quadrants can be treated analogously.

A similar approach can be used in three space dimensions [34, 33] but the body surface is defined using a conformal surface triangulation. In this surface triangulation has only to be of sufficient quality to give an accurate body representation as it is not used directly to discretise the flow solution, representations obtained from CAD systems are thus normally appropriate.

For a finite volume method the direction of the outward pointing normal must be known for each solid face and, the area of each uncut cell face and the uncut volume of the cell must be determined. In the original implementation 16 cut cell types [31, 32] were used to compute this geometric information. In the three dimensional solver vector algebra has been used [33, 34]. The fluid area of the cell sides can be calculated based on the intersection points at the cell edges. If the solid face is now approximated by a non-planar quadrilateral, its normal vector and area can be computed using

$$|\mathbf{S}| = \sqrt{(S_x^L - S_x^R)^2 + (S_y^L - S_y^R)^2 + (S_z^L - S_z^R)^2} \tag{2}$$

$$\mathbf{n} = \frac{1}{|\mathbf{S}|} \begin{pmatrix} S_x^R - x^L \\ S_y^R - S_y^L \\ S_z^R - S_z^L \end{pmatrix} \tag{3}$$

$$V = \frac{1}{3} \sum_{i=1}^{M} \mathbf{P}_i . \mathbf{n}_i S_i \tag{4}$$

where S_{xyz}^{LR} is the left or right face of the Cartesian grid cell when viewed from the x,y or z direction, $\mathbf{P}_i$, $\mathbf{n}_i$ and S_i are the centroid, normal vector and area of the i^{th} face of the cell. In Cieslak et al's [34] implementation an arbitrary number of cuts to one cell is permitted.

Within the Cartesian cut cell method it is necessary to use a finite volume flow solver which is based on conducting a flux balance around the edges of the cell. This approach allows the unusual number of edges which occur in cut cells to be considered. In MMU's shallow water codes the solver [35, 45] is based on the second order MUSCL-Hancock [46] solver, though this is not the only possible scheme. LeVeque and Shyue [39] used a large time-step version of Roe's solver as does the AMAZON-SC code [44], while Tucker and Pan [37] use the CONDIF scheme [47]. In all approaches, however, the vast majority of the grid is treated using the simplest possible implementation of the chosen solver, i.e. the Cartesian form.

2.1.1 Cell Merging

In practice, cut cells may be arbitrarily small and some technique must be employed to overcome time step stability restrictions associated with explicit methods. A cell merging technique [48, 49] may be implemented where small cells (i.e. cells with a fluid area $A_{ij} < A_{min}$) are combined, so that the global time step is not restricted. The cell to merge with is usually selected by finding that neighbouring cell lying in the direction of the normal vector to the solid face. The choice of A_{min} is based on a trade off between time step and geometric resolution, normally $A_{min} = 0.5\Delta x \Delta y$ is considered to be acceptable [50]. An alternative approach is to use a method which is stable for large time steps [39].

2.2 Free surface capturing method

A two-fluid solver has been developed which can be applied to a variety of problems with free surfaces based on the surface capturing scheme and a novel Cartesian cut cell approach [45, 36]. More specifically, the mathematical model of an immiscible two-fluid system is formulated as a set of partial differential equations which govern the motion of an inviscid, incompressible, variable density fluid. These equations consist of a mass conservation

(density) equation (which is mathematically equivalent to the volume fraction transport equation), momentum equation and an incompressibility constraint that are solved simultaneously using the finite volume method. The formulation is based on the artificial compressibility method [51, 52, 53, 54, 36] in which the pressure, density and velocity fields are directly coupled to produce a hyperbolic system of equations. To achieve a time-accurate solution for unsteady flow problems an implicit dual-time iteration technique has been used [52, 53] in which the solution at each real time step is obtained by solving a steady-state problem in a pseudo-time domain. To evaluate the inviscid fluxes, Roe's flux function is adopted locally at each cell interface assuming a 1-D Riemann problem in the direction normal to the cell face. To achieve a second-order accurate solution in space, a piecewise linear model for the stored cell centre variables is used in conjunction with a slope limiter to prevent over-shoots or under-shoots in the interpolated data at cell interfaces before the two Riemann states are computed. At the pseudo-time iteration level, however, a first order upwind scheme is sufficient to calculate the inviscid fluxes and the resultant linear equations are solved using an approximate LU factorisation scheme [55]. At every real time step, once the flow variables including density have been calculated, the position of the material interface can be defined as the contour with the average density value of the two fluids. A number of different boundary conditions including inlet, outlet (open boundary) and solid walls are implemented to facilitate the applications to real flow problems. Complex geometries [45, 44] arising in real coastal engineering problems can be easily represented by cut cells which provide a fully boundary-fitted mesh capability without any mesh generation in the conventional sense. A novel scheme has also been proposed for the accurate treatment of the pressure gradient term within the free surface capturing method for flows under the influence of gravity [56]. The vertical pressure gradient term is split into hydrostatic and kinematic pressure gradient terms which are then calculated separately in order to exactly balance the gravity source term in each cell.

2.3 Numerical Method

2.3.1 Governing equations and boundary conditions

The integral form of the 2-D incompressible Euler equations for a fluid system with variable density field can be written as

$$\frac{\partial}{\partial t}\int\int_{\Omega}\mathbf{Q}\,d\Omega+\oint_{S}\mathbf{F}\cdot\mathbf{n}\,ds=\int\int_{\Omega}\mathbf{B}\,d\Omega \tag{5}$$

where Ω is the domain of interest, S is the boundary surrounding Ω, $\mathbf{n}$ is the unit normal to S in the outward direction, $\mathbf{Q}$ is the vector of conserved variables, $\mathbf{F}$ is the vector of flux function through S and $\mathbf{B}$ is the source term for body forces. These equations in order are the mass conservation (density) equation, x-direction momentum equation, y-direction momentum equation and incompressibility constraint (continuity equation). It can be shown that the density equation is in fact the basis for deriving the volume fraction equation in the well known VoF method [11]. By using the artificial compressibility method and assuming the only body force is the gravity, $\mathbf{Q}$, $\mathbf{F}$ and $\mathbf{B}$ are given as $\mathbf{Q}=[\rho,\rho u,\rho v,p/\beta]^T$, $\mathbf{F}=f^I\mathbf{n}_x+g^I\mathbf{n}_y$ and $\mathbf{B}=[0,0,-\rho g,0]$, where $f^I=[\rho u,\rho u^2+p,\rho uv,u]^T$, $g^I=[\rho v,\rho uv,\rho v^2+p,v]^T$, $\mathbf{n}_x$ and $\mathbf{n}_y$ are the unit vectors along x- and y-directions respectively, u and v are the velocity components, ρ is the density, p is the pressure, β is the coefficient of artificial compressibility and g is the gravitational acceleration.

Introducing a fictitious time derivative of pressure into the continuity equation produces a system of hyperbolic equations which can then be solved by any of the recently developed upwind finite volume techniques, such as the characteristics-based Godunov-type schemes. Clearly, from the above formulation, any meaningful solution can only be achieved when a divergence-free velocity field is recovered, i.e. $\partial p/\partial t\rightarrow 0$. For a steady-state calculation, this should not be a problem. For unsteady flow problems, however, a divergence-free

velocity should be attained at every time step, which can be achieved by using the dual-time stepping technique and sub-iterating the equations in the pseudo-time domain to achieve a steady-state solution at each physical time step.

The boundary conditions encountered in the hydraulic flow problems implemented in the present study can be classified as

i) inlet: At this boundary, the velocity and density distributions are specified. The pressure is unknown and a boundary value is extrapolated from the interior of the flow domain.

ii) outlet or open boundary: The pressure at this boundary is fixed and a zero gradient condition is applied to the velocity and density. This definition allows fluids to freely enter or leave the computational domain according to the local flow velocity and direction.

iii) solid wall boundary: At this boundary, the no-penetration condition can be applied to the velocity and the density is assumed to have a zero normal gradient. For the pressure, if the wall is stationary, we have $\nabla p = [0, -\rho g]$.

iv) seaward boundary: the desired waves must propagate into the solution domain through this boundary, whilst any reflected waves should pass out. This boundary is implemented by specifying the velocity of the water through the boundary. The velocity (as a function of local water depth) is obtained using a JONSWAP spectrum together with linear wave theory. The instantaneous water velocity at a depth, z, below the still water level, h, is found by linear superposition of the sampled waves, i.e.

$$u(x,z,t) = \sum_i a_i \omega_i \frac{\cosh k_i(h+z)}{\sinh k_i h} \sin(\omega_i t - k_i x), \tag{6}$$

$$v(x,z,t) = \sum_i a_i \omega_i \frac{\sinh k_i(h+z)}{\sinh k_i h} \cos(\omega_i t - k_i x), \tag{7}$$

where a_i is the amplitude of the i^{th} component, k_i is the wave number of the i^{th} component, $\omega_i/(2\pi)$ is the frequency of the i^{th} component, h is the local water depth, ω and k are related by $\omega^2 = gk\tanh(kh)$. Full details of this methodology are given in "Linear Wave Theory" by HE Krogstad and ØA Arntsen, Norwegian University of Science and Technology, Trondheim, which is published on the web.

2.3.2 Numerical solution

In the present study, a cell centred finite volume approach has been adopted to discretise the governing equations on uniform Cartesian grids. For each control volume (i,j), (5) can be written as

$$\frac{\partial \mathbf{Q}_{i,j} V_{i,j}}{\partial t} = -\oint_{\partial C_{i,j}} \mathbf{F}\cdot\mathbf{n}\, ds + \mathbf{B} V_{i,j} = -R(\mathbf{Q}_{i,j}) \tag{8}$$

where $\mathbf{Q}_{i,j}$ are the average quantities at cell (i,j) stored at the cell centre, and $\partial C_{i,j}$ and $V_{i,j}$ denote the boundary of the cell and area of cell i,j, respectively. The surface integration on the right hand side of (8) is evaluated by summing the flux vectors over each edge of a cell and the discrete form of the integral is

$$\oint_{\partial C_{i,j}} \mathbf{F}\cdot\mathbf{n}\, ds = \sum_{k=1}^{m} F_k \Delta l_k \tag{9}$$

where m is the number of the faces of cell (i,j), F_k is the numerical flux through edge k of cell (i,j), and Δl_k is the length of the edge. In AMAZON-SC, each cell has four faces $(m=4)$, unless it is cut in which case it may have three, four or five faces.

In order to evaluate the inviscid numerical fluxes F_k^I, Roe's flux function is adopted locally at each cell edge, assuming a 1D Riemann problem in the direction normal to the cell edge, as follows:

$$F_k^I = \frac{1}{2}[F^I(\mathbf{Q}_k^+) + F^I(\mathbf{Q}_k^-) - |A|(\mathbf{Q}_k^+) - \mathbf{Q}_k^-)], |A| = R|\Lambda|L, \tag{10}$$

where $\mathbf{Q}_k^+$ and $\mathbf{Q}_k^-$ are the reconstructed right and left states at face k of cell (i,j) , A is the flux Jacobian evaluated by Roe's average state. The quantities R, L and Λ are the right and left eigenvectors of A and the eigenvalues of A [7].

To achieve second-order accuracy, a piecewise linear model for the cell variables must first be reconstructed from the solution before the two Riemann states at each cell edge are computed. For a given cell with centre point (i,j) for example, this requires the construction of the cell variables in the form

$$\mathbf{Q}(x,y) = \mathbf{Q}_{i,j} + \nabla\mathbf{Q}_{i,j} \cdot \mathbf{r} \tag{11}$$

where $\mathbf{r}$ is the vector from the cell centre to any point (x,y) within cell (i,j), $\mathbf{Q}_{i,j}$ is the cell centre data at the cell, and $\Delta\mathbf{Q}_{i,j}$ is the gradient of solution data at cell (i,j) evaluated using the neighbouring cell centre values, i.e.

$$\nabla\mathbf{Q}_{i,j} = G[\frac{\mathbf{Q}_{i+1,j} - \mathbf{Q}_{i,j}}{\Delta x}, \frac{\mathbf{Q}_{i,j} - \mathbf{Q}_{i-1,j}}{\Delta x}]\mathbf{n}_x + G[\frac{\mathbf{Q}_{i,j+1} - \mathbf{Q}_{i,j}}{\Delta y}, \frac{\mathbf{Q}_{i,j} - \mathbf{Q}_{i,j-1}}{\Delta y}]\mathbf{n}_y \tag{12}$$

where G is a slope limiter function which is used to prevent over- or under-shoots. The limiter function, among others, may take one of the following forms:

- The van Leer limiter

$$G(a,b) = \frac{a|b| + |a|b}{|a| + |b|} \tag{13}$$

- The super-bee limiter

$$G(a,b) = s \cdot \max[0, \min(2|b|, s \cdot a), \min(|b|, 2s \cdot a)] \tag{14}$$

  where $s = \text{sign}(b)$.

By discretising (8) in time and omitting the subscripts for simplicity, the first-order Euler implicit difference scheme for example can be used:

$$\frac{(\mathbf{Q}V)^{n+1} - (\mathbf{Q}V)^n}{\Delta t} = -R(\mathbf{Q}^{n+1}), \tag{15}$$

where V is the cell area. To achieve a time-accurate solution for each time step for unsteady flow problems, (15) must be further modified to obtain a divergence free velocity field. This is accomplished by introducing a pseudo-time derivative into the system of equations, as

$$\frac{(\mathbf{Q}V)^{n+1,m+1} - (\mathbf{Q}V)^{n+1,m}}{\Delta\tau} + I_{ta}\frac{(\mathbf{Q}V)^{n+1,m+1} - (\mathbf{Q}V)^n}{\Delta t} = -R(\mathbf{Q}^{n+1,m+1}), \tag{16}$$

where τ is the pseudo-time and $I_{ta} = diag[1,1,1,0]$. The right-hand side (RHS) of (16) can be linearised using Newton's method at the $m+1$ pseudo-time level to yield

$$\begin{aligned}[I_m V + \frac{\partial R(\mathbf{Q}^{n+1,m})}{\partial \mathbf{Q}}](\mathbf{Q}^{n+1,m+1} - \mathbf{Q}^{n+1,m}) \\ = -[I_{ta}\frac{(\mathbf{Q}^{n+1,m} - \mathbf{Q}^n)V}{\Delta t} + R(\mathbf{Q}^{n+1,m})],\end{aligned}$$

where $I_m = diag[1/\Delta\tau + 1/\Delta t, 1/\Delta\tau + 1/\Delta t, 1/\Delta\tau + 1/\Delta t, 1/\Delta\tau]$. When $\Delta(\mathbf{Q}^{n+1})^m = \mathbf{Q}^{n+1,m+1} - \mathbf{Q}^{n+1,m}$ is iterated to zero, the density and momentum equations are satisfied

and the divergence of the velocity at time level $n+1$ is zero. The system of equations can be written in matrix form as

$$(D + L + U)\Delta\mathbf{Q}^s = RHS, \tag{17}$$

where D is a block diagonal matrix, L is a block lower triangular matrix, and U is a block upper triangular matrix. Each of the elements in D, L and U is a 4×4 matrix. An approximate LU factorisation(ALU) scheme as proposed by Pan and Lomax [55] can be adopted to form the inverse of (16) in the form

$$(D + L)D^{-1}(D + U)\Delta\mathbf{Q}^s = RHS. \tag{18}$$

Within each time step of the implicit integration the sub-iteration is terminated when the L_2 norm of the iteration process

$$L_2 = \left(\frac{1}{N} \sum_{i}^{N} \left(\mathbf{Q}^{s+1} - \mathbf{Q}^s \right)^2 \right)^{\frac{1}{2}}, \tag{19}$$

is less than a specified limit.

2.4 Extension for rubble mound breakwaters

In order to extend the solver to deal with rubble mound structures a porosity model must be included. In order to achieve this the body force term of the Navier-Stokes equations is extended to include terms modelling the porosity, using the method proposed by Huang et. al. [57].

$$\mathbf{B} = \begin{pmatrix} 0 \\ -\frac{\nu N_w}{K_p} u - \frac{C_f N_w^2}{\sqrt{K_p}} u\sqrt{u^2+v^2} \\ -\frac{\nu N_w}{K_p} v - \frac{C_f N_w^2}{\sqrt{K_p}} v\sqrt{u^2+v^2} - \rho g \\ 0 \end{pmatrix} \tag{20}$$

Where the frictional losses associated with the porous structure are parametrised using the three following quantities; K_p (m^2) is the permeability coefficient of the structure, N_w is the, dimensionless, intrinsic porosity of the structure, and, C_f is a dimensionless turbulent resistance associated with the structure. In general N_w is a design parameter of the structure and is known along with a nominal diameter d_n of the rubble.

Various correlations exist for computing K_p McDougall, quoted by Huang et al [57], recommends using

$$K_p = 1.643 \times 10^{-7} \left(\frac{d_n}{d_0} \right)^{1.57} \frac{N_w^3}{(1 - N_w)^2} \tag{21}$$

where $d_0 = 10\mathrm{mm}$.

The turbulent resistance may be determined using the correlation proposed by Arbhabhiramar and Dinoy [58],

$$C_f = 100 \left(d_n \sqrt{\frac{N_w}{K_p}} \right)^{-1.5}. \tag{22}$$

To complete the numerical solution the intrinsic permeability and porosity coefficients are stored for each grid cell in the computational domain. The additional terms in the body force vector are then computed for each porous grid cell. Rubble mound structures are thus represented by defining a region of grid cells with non-zero N_w.

2.4.1 A test case for porous media

In order to test the implementation of the porosity model described in Section 2.4 the solver has been applied to the test case described by [59] and shown in Figure 2. A porous block with height $0.5H$ is located at $7.5H$ away from the left boundary of a two dimensional horizontal channel with height H and length $58H$, respectively. The downstream part of the channel ($50H$) is long enough for the fully developed distributions of the velocity to be obtained. The velocity is prescribed at the left hand (inlet) boundary to ensure a fully developed parabolic distribution with average value u_0, i.e. $u = 6y(1-y)$. In the present case u_0 is chosen to ensure an inlet Reynolds number of 500, the porosity of the porous block is 0.5 and the particle diameter is $0.05H$ ($H = 1.0$m is specified for the test).

Figure 3 shows the computed velocity vectors, for the entire domain, from the simulation. The recovery of a fully developed profile at the exit and the recirculation region behind the porous media are clearly visible. The horizontal and vertical velocity distributions along the interfacial surfaces of the porous block are shown in Figure 4. Due to the large porosity on the media, most of the fluid flows through the porous block via the upper left corner, where the maximum velocity is observed. Comparisons with the published results for this test case (Figure 5) are favourable with the slight differences observed being due to the fact that present results are based on a collocated method whilst the published results utilize a staggered grid.

2.5 Wave run up and over-topping on a smooth sea dike

In order to provide a direct comparison with VoFbreak^2, AMAZON-SC has been applied to the test case of wave run up on a smooth sea dike with a 1:6 front face. The test conditions are exactly as described by Troch et al [14] with a still water level of 0.7m and random waves generated from the JONSWAP spectrum, with $H_s = 0.16$m and $T_P = 2$s. Numerical wave gauges were positioned 0.01m, 1.00m (co-located with the toe of the structure) and 3.81m from the seaward boundary. The computation was performed on a grid of 200×100 cells with a uniform mesh spacing of 0.0315m in the horizontal direction and 0.01m in the vertical direction. Figure 6 shows the computed density profiles between 4.2 and 7.1 seconds, a period which equates to approximately one and a half wave periods. In the plots a linear colour scale is used from red (air; density 1.0) to blue (water; density 1000.0). The plot at 4.2 seconds shows the down-wash of the proceeding wave just as it is withdrawing from the crest of the dike. By 4.8 seconds the next wave is approaching the dike and its height can be seen to have increased as it shoals on the front face. The plots at 5.4 and 6.0 seconds show this wave breaking on the upper reaches of the dike and by 6.5 seconds an over-topping jet can clearly be seen. The final plot at 7.4 seconds shows the wave starting to retreat. The processes observed in these plots are similar to those predicted by VoFbreak^2 (Figure 30). Finally figure 7 shows the output from two numerical wave gauges located 1.0 metres (at the toe of the dike) and 3.81 metres from the seaward boundary, these plots clearly show the effect of the slope on the waves.

2.6 Samphire Hoe

The Amazon-SC code has been applied to examine selected wave over topping events at Samphire-Hoe to help asses the impact of scale effects. The computational domain, geometry of the sea wall and the locations of the numerical wave gauges is shown in Figure 8. This test section is identical to that modelled in the Edinburgh experiments conducted under Workpackage 4 of the CLASH project [60]. The armour at the toe of the structure consists of fairly angular, 4 ton, narrowly graded rock with a dn_{50} of around 1.5m (see Figure 9). The considered opinion of the HR-Wallingford team is that the porosity of the toe is approximately $N_w = 35\%$ and that consequently, using equation (21), $Kp = 4.35 \times 10^{-5}\,\mathrm{m}^2$, while $C_f = 0.06407$.

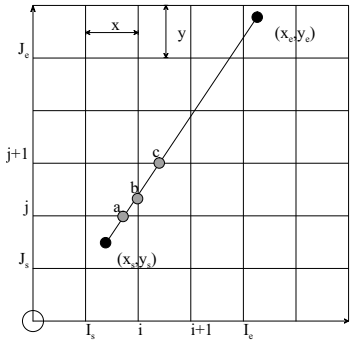

Figure 1: Finding cut cells: Locating the intersection points of a line segment

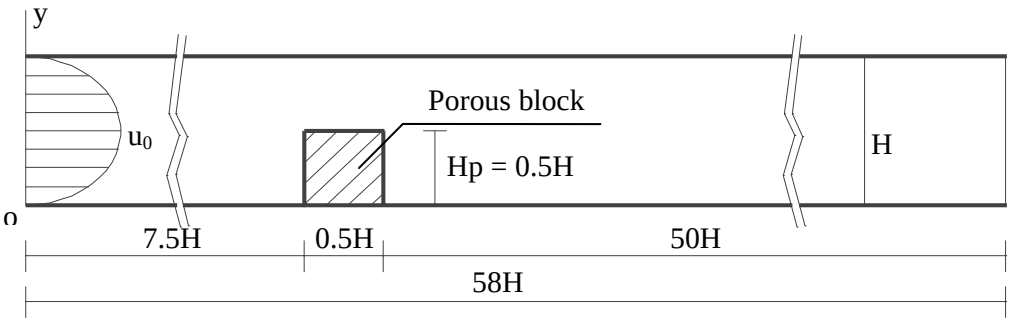

Figure 2: Computational domain for the porous media test case

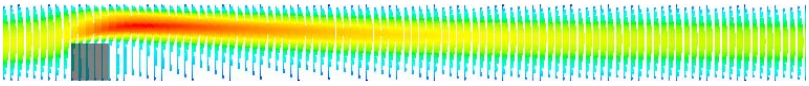

Figure 3: Porous media test: Velocity vectors for the whole domain, showing fully developed flow at the outlet

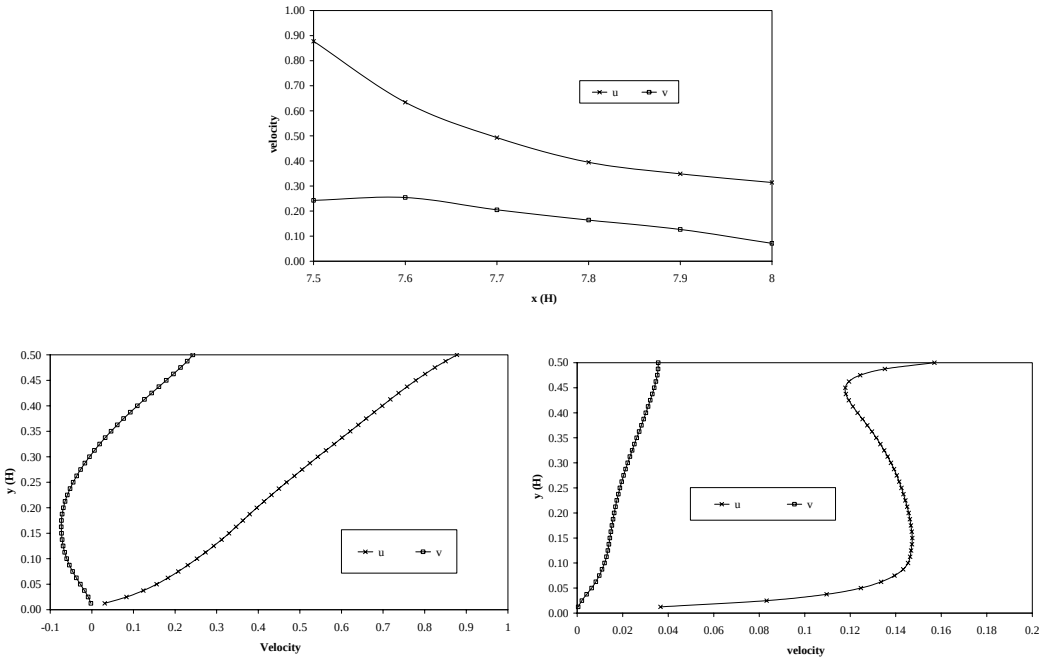

Figure 4: Porous media test: Horizontal and vertical velocity distributions on interfacial surfaces of the porous block: top, left and right sides respectively

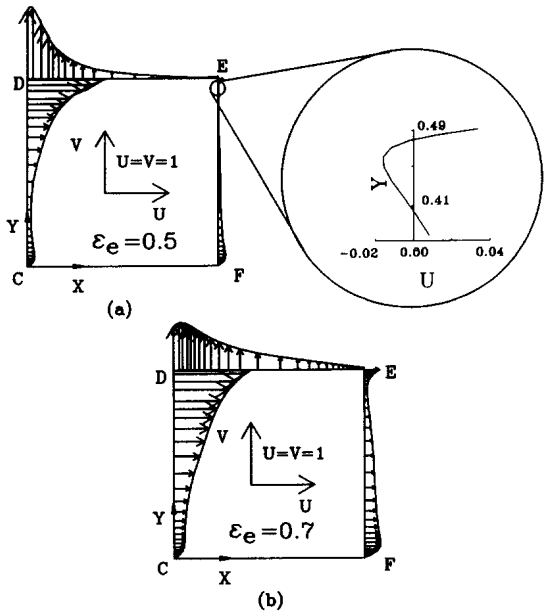

Figure 5: Nominal velocity distributions on the interfacial surface of the porous block ($R_e = 500$, $HP = 0.5$, $P_r = 0.7$ and $D_p = 0.1$): (a) $\epsilon_e = 0.5$ and (b) $\epsilon_e = 0.7$, reprinted from Fu et. al. [59]

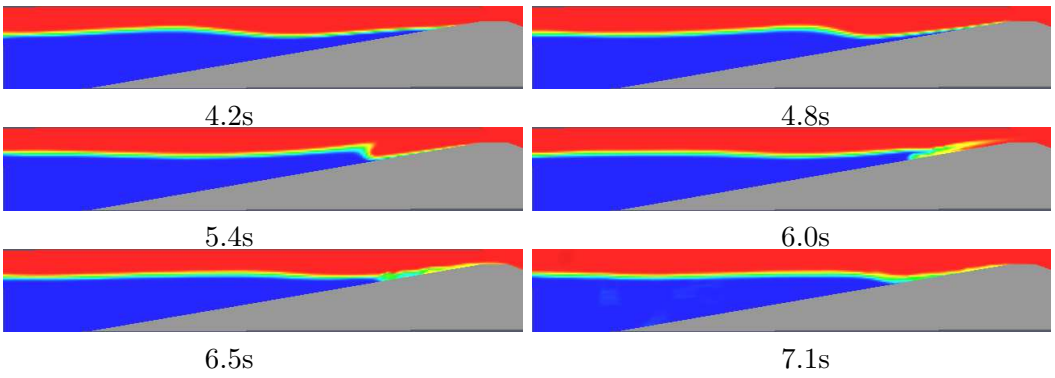

Figure 6: Numerical wave flume simulation of wave run-up and over-topping of a smooth sea-dike: density profiles at between 4.2 and 7.1 seconds.

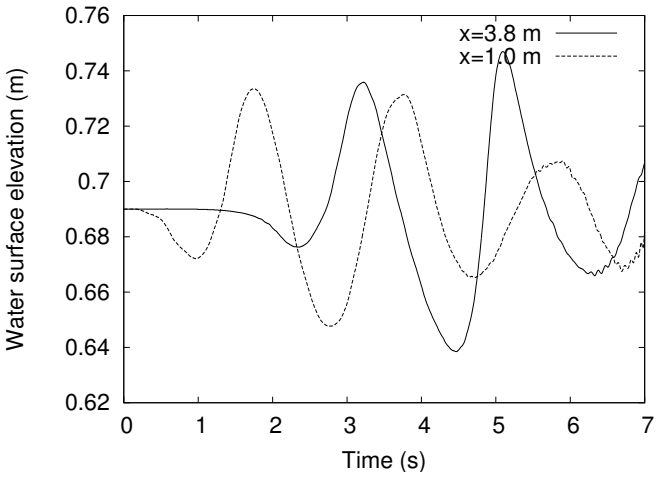

Figure 7: Numerical wave flume simulation of wave run-up and over-topping of a smooth sea-dike: Water surface elevation histories for wave gauges located 1.0m and 3.81m from the seaward boundary.

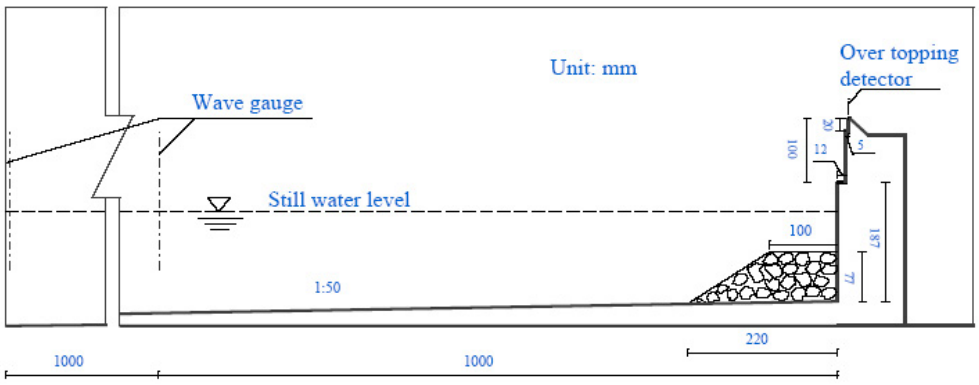

Figure 8: Samphire Hoe: Overview of the test section

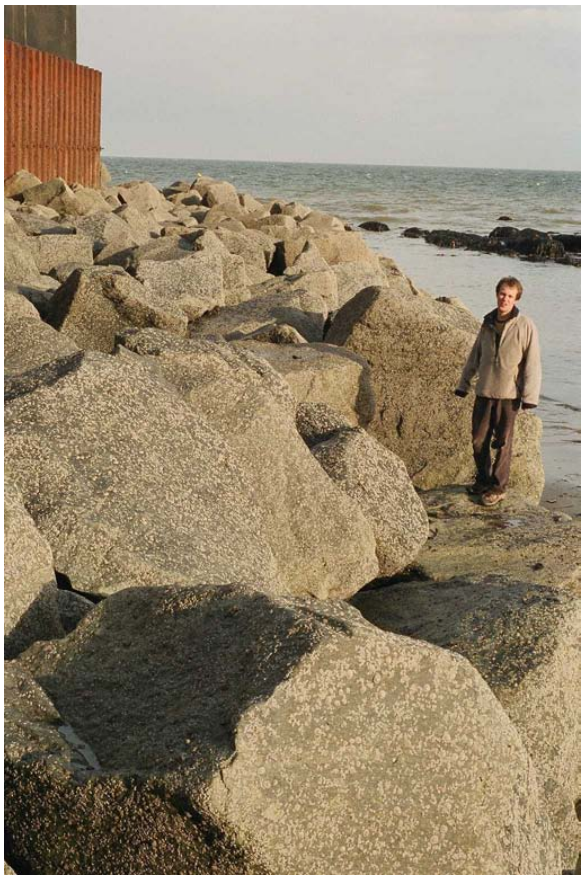

Figure 9: Samphire Hoe: Exposed rock toe at low tide (Courtesy of T Pullen, HR-Wallingford)

Data for two runs of the experiment have been received from Edinburgh University (3010OT10 and 3010OT17). The design conditions for these tests are shown in Table 1. Both tests have similar dimensionless freeboards but in the first test the waves have a slightly longer period in slightly shallower water. The wave climates at the wave gauge 2m from the toe of the structure were analysed, for both tests, using the WaveLab-2 software from Aalborg University in order to provide information for the seaward boundary conditions. This is a necessary step since the design conditions shown in Table 1 are the conditions which would exist at the toe of the structure without the structure in-place, (Figure 10) shows the spectra obtained for each test case. The detailed analysis is shown in Figures 11 and 12 while Table 2 shows the results of the time series analysis.

In order to simulate the 3010OT10 test, a series of random waves at the seaward boundary has been generated using the JONSWAP spectrum with the same spectral parametres as those identified in the Wavelab analysis (e.g. $T_p = 0.9416$s and $H_s = 0.1037$m). The resulting time series was examined for significant event and the simulation was started at an appropriate time. Figure 14 shows the interaction of two large waves with the seawall over a five second period. The second wave results in an overtopping event, which occurs between 3.44 and 3.5 seconds after the start of the simulation. During this event 0.033 lm^{-1} overtops the wall, which at prototype scale equates of an instantaneous discharge of 1.32 lm^{-1}. This low overtopping discharge is composed almost entirely of spray and results from the wave breaking near the toe of the rubble mound. Repeating the simulations at a model scale of 1:20 (i.e. twice the laboratory scale) show almost identical behaviour indicating that for the tested flow conditions the turbulent effects of the rubble mound structure are negligible. This conclusion is in agreement with the results obtained when comparing both the model tests, field measurements and the Besley curve.

Table 1: Samphire Hoe: Design conditions for the Edinburgh Experiments (curtsey of T Bruce and J Pearson).

Test	h	R_c	d	H_s^*	T
3010OT10	0.140	0.147	0.0627	0.052	0.941
3010OT17	0.145	0.142	0.0674	0.064	0.921

Table 2: Samphire Hoe: Wavelab time series analysis of experimental data for the gauge 2m from the wall.

	No.	Frequency Domain					Time Domain		
Test	waves	H_{m0}	T_p	$T_{-1,0}$	$T_{0,1}$	$T_{0,2}$	H_m	T_m	H_s
3010OT10	1187	0.1069	0.9416	0.914	0.8712	0.843	0.06575	0.862	0.1037
3010OT17	1253	0.1198	0.8715	0.8412	0.8077	0.7849	0.07777	0.817	0.1122

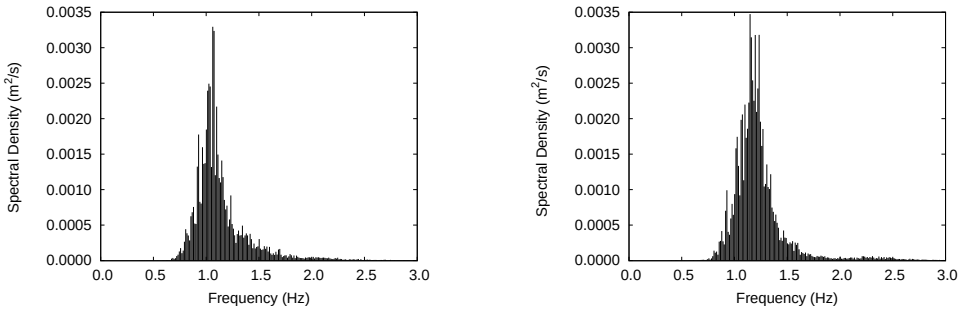

Figure 10: Samphire Hoe: Wave power spectrum from at gauge 2.0m from the wall in the Edinburgh experiments: 3010T10 (left) and 3010T17 (right).

Time Series Analysis - Wave Elevations

Input Parameters

Generel

Data file:	D:\...\edinburgh data\3010OT10.dat
Sample frequency:	100 Hz
Length scale (Prototype/Model):	1
Channel number:	2
Calibration coefficient (m/V):	0.02
Skipped lines	Header: 0 Start: 0 End: 0

Bandpass filtering

Freq. lower bound:	0.354 Hz
Freq. upper bound:	3.186 Hz

Frequency Domain Analysis

Overlap of subseries:	20%
Cosine taper width:	20%
Data No. in FFT block:	8192
Number of FFT blocks:	15

Time Domain Analysis

Min. points between downcrossings:	28
Hilbert filter length:	4096

Frequency Domain Analysis

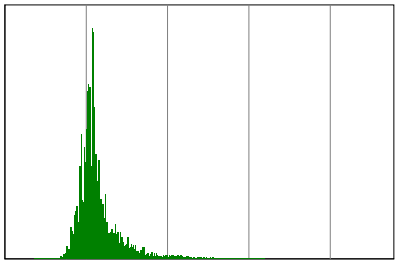

Sig. wave height H_{m0}(m):	0.1069
Peak wave period T_p (s):	0.9416
Mean wave period $T_{-1,0}$ (s):	0.914
Mean wave period $T_{0,1}$ (s):	0.8712
Mean wave period $T_{0,2}$ (s):	0.843
Spectral Width (Broadness):	0.5552
Spectral Width (Narrowness):	0.2608

Time Domain Analysis

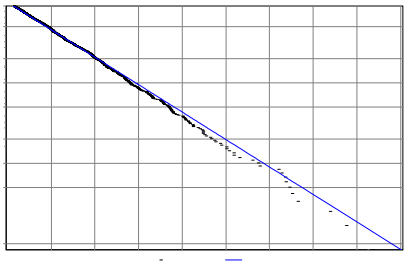

Number of waves:	1187
Mean wave height H_m(m):	0.06575
Mean wave period T_m(s):	0.862
Sig. wave height H_s (m):	0.1037
$T_{H_{1/3}}$ (s):	0.9127
Sig. wave period T_s (s):	1.057
H_{max} (m):	0.1901
T_{Hmax} (s):	0.9952
$H_{1/10}$ (m):	0.1303
$H_{1/50}$ (m):	0.1584
$H_{1/100}$ (m)	0.1694
$H_{1/250}$ (m):	0.1779
$H_{0.1\%}$ (m):	0.1888
$H_{1\%}$ (m):	0.1577
$H_{2\%}$ (m):	0.1424
$H_{10\%}$ (m)	0.1424
Groupiness factor GF:	1.047

Department of Civil Engineering

Aalborg University

Project title	Samphire Hoe
Drawn by	DMI
Date	1. Sep 2004
Remarks	Analysis of the Edinburgh Data
Page	1 of 1

Figure 11: Wavelab time series analysis of the experimental measurements at gauge 2 for the 3010OT10 test.

Time Series Analysis - Wave Elevations

Input Parameters

Generel

Data file:	*D:\...\edinburgh data\3010OT17.dat*
Sample frequency:	*100 Hz*
Length scale (Prototype/Model):	*1*
Channel number:	*2*
Calibration coefficient (m/V):	*0.02*
Skipped lines	*Header: 0 Start: 0 End: 0*

Bandpass filtering

Freq. lower bound:	*0.382 Hz*
Freq. upper bound:	*3.442 Hz*

Frequency Domain Analysis

Overlap of subseries:	*20%*
Cosine taper width:	*20%*
Data No. in FFT block:	*8192*
Number of FFT blocks:	*15*

Time Domain Analysis

Min. points between downcrossings:	*26*
Hilbert filter length:	*4096*

Frequency Domain Analysis

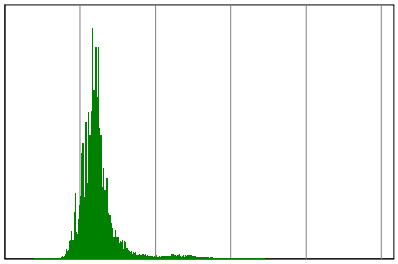

Sig. wave height H_{m0}(m):	*0.1198*
Peak wave period T_p (s):	*0.8715*
Mean wave period $T_{-1,0}$ (s):	*0.8412*
Mean wave period $T_{0,1}$ (s):	*0.8077*
Mean wave period $T_{0,2}$ (s):	*0.7849*
Spectral Width (Broadness):	*0.5394*
Spectral Width (Narrowness):	*0.243*

Time Domain Analysis

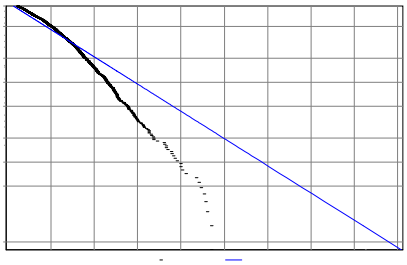

Number of waves:	1253
Mean wave height H_m(m):	*0.07777*
Mean wave period T_m(s):	*0.817*
Sig. wave height H_s (m):	*0.1122*
$T_{H_{1/3}}$ (s):	*0.8507*
Sig. wave period T_s (s):	*0.9612*
H_{max} (m):	*0.1687*
T_{Hmax} (s):	*0.8992*
$H_{1/10}$ (m):	*0.1328*
$H_{1/50}$ (m):	*0.1554*
$H_{1/100}$ (m)	*0.1619*
$H_{1/250}$ (m):	*0.1672*
$H_{0.1\%}$ (m):	*0.1687*
$H_{1\%}$ (m):	*0.1545*
$H_{2\%}$ (m):	*0.1426*
$H_{10\%}$ (m)	*0.1426*
Groupiness factor GF:	*0.818*

Department of Civil Engineering

Aalborg University

Project title	*Samphire Hoe*
Drawn by	*DMI*
Date	*1. Sep 2004*
Remarks	*Analysis of the Edinburgh Data*
Page	*1 of 1*

Figure 12: Wavelab time series analysis of of the experimental measurements at gauge 2 for the 3010OT17 test.

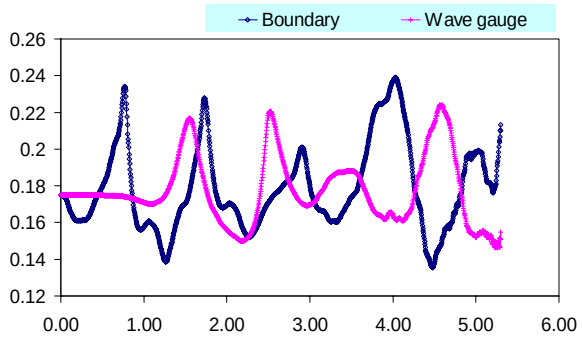

Figure 13: Samphire Hoe: Computed elevation time series at the wave gauges 2m and 1m from the seawall (3010OT10 test).

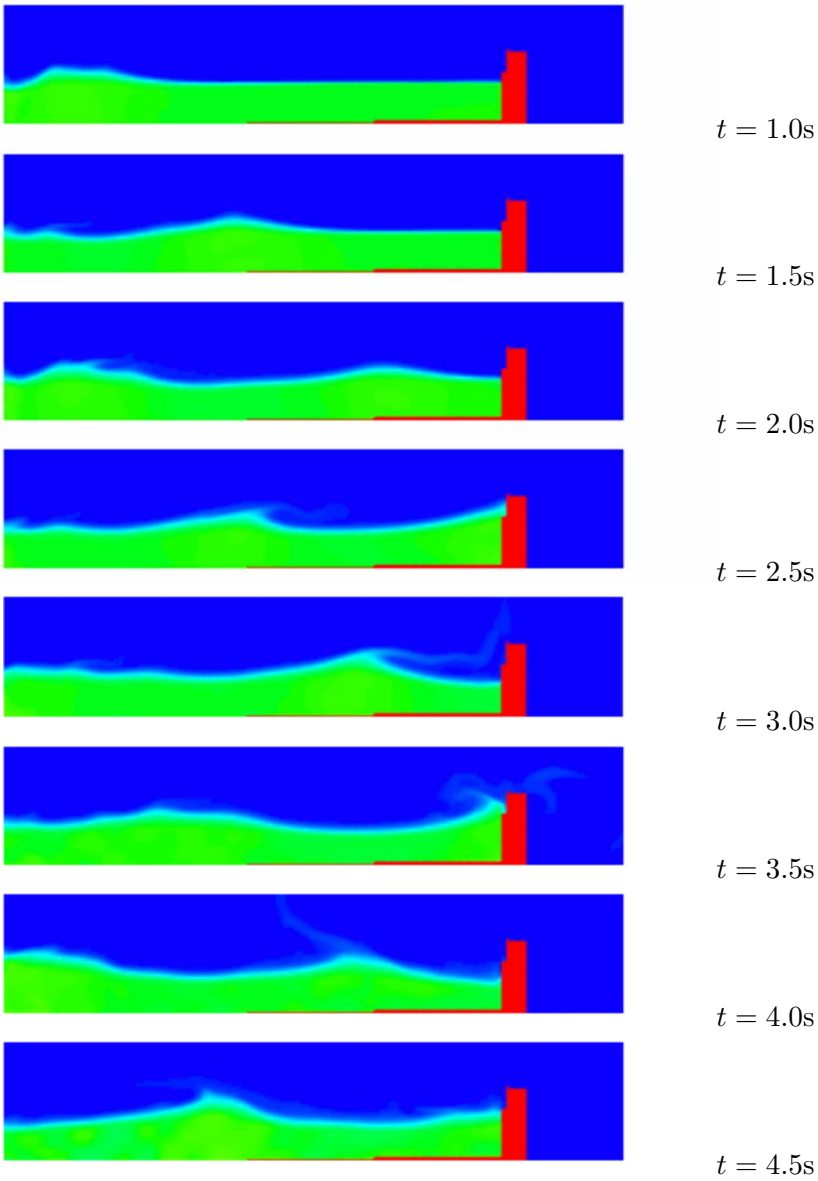

Figure 14: Samphire Hoe: Computed water surface profiles (3010OT10 test)

3 Assessment of Scale Effects

It was reported at the last CLASH workshop that the measured volumes in laboratory simulations of overtopping on the rough porous breakwaters at Zeebrugge and Ostia are much lower than those observed in the prototype measurements. It is clear that either Froude scaling is not valid for these structures or that wind plays a significant part. Experiments have been conducted at UPV to investigate the effects of wind at Zeebrugge, whilst the work in this proposal aims to examine the effects of scale.

It is well known that the body force associated with pressure losses due to friction for flow in an open channel is;

$$F_f = \frac{f}{d_h}\frac{1}{2}\rho u^2. \tag{23}$$

where d_h is the hydraulic diameter of the channel.

For Laminar flow the friction factor, f, depends only on the Reynolds Number, Re. As the flow becomes turbulent, however, Colebrook's semi-empirical correlation must be used. Colebrook's formulation depends not only on the Reynolds number but also on the relative roughness of the material, ϵ/d_h. Colebrook's correlation for the friction factor in turbulent pipe flow is

$$f^{-\frac{1}{2}} = -2\log\left(\frac{2.51}{Re.f^{\frac{1}{2}}} + \frac{\epsilon/d_h}{3.70}\right). \tag{24}$$

The Reynolds number is defined as

$$Re = \frac{\rho u d_h}{\mu} \tag{25}$$

where μ is the dynamic viscosity.

When Froude scaling is applied to overtopping on a rough structure the relative roughness probably scales correctly as the thickness of the overtopping jet, d, is expected to scale with according to the Froude law, whilst the length scale of the armour layer, ϵ, is a characteristic length and will have been scaled accordingly. Unfortunately the viscosity of the fluid will not have been scaled so, even if, the characteristic velocity of the overtopping jet scales with the Froude law the Reynolds number will be different.

Work on smooth and rough dikes [61] has shown that provided the model and prototype structures are both in regimes with high enough Reynolds numbers, f, can be considered to be constant. Figure 15 shows the friction factor against Reynolds number for $\epsilon/d = 0.001$, and it can clearly be seen that for Reynolds numbers of above 10^5 the friction factor could be considered constant. This is also supported by investigations of Sakakiyama & Kajima [62] on a seawall covered with armour stones who have suggested the same value. Overtopping tests by the same authors [63] have shown smaller overtopping rates in the model as compared to the field. All investigations showed that the hydraulic resistance in the model is larger than in the field so that smaller run-up heights and smaller overtopping volumes are achieved in the model.

Following the 5^{th} project workshop (held in Edinburgh) the MMU team proposed to use their AMAZON-SC solver to perform a number of simulations on a rough, porous structure, at various scales in order to determine the typical thickness and velocity of the overtopping jet and thus estimate the friction factor associated with each case and thus show the effects of scaling. In order to provide an understanding of the physics a simple structure would be tested under regular wave conditions. The proposed structure would, at model scale, consist of a porous breakwater (K=0.56, Nw=35%), 0.7m tall with 1:3 front face, consisting of ten, 10cm tall steps (to simulate an armour layer). Behind the porous face will be a solid, impermeable region, 0.8m tall. The breakwater will be subjected to 0.16m high regular waves with a period of 2.0s. Overtopping will be measured across the crown of the structure and the numerical study will allow measurements of the jet velocity and jet thickness to be measured. The calculations would be repeated at scales of 2:1, 5:1,

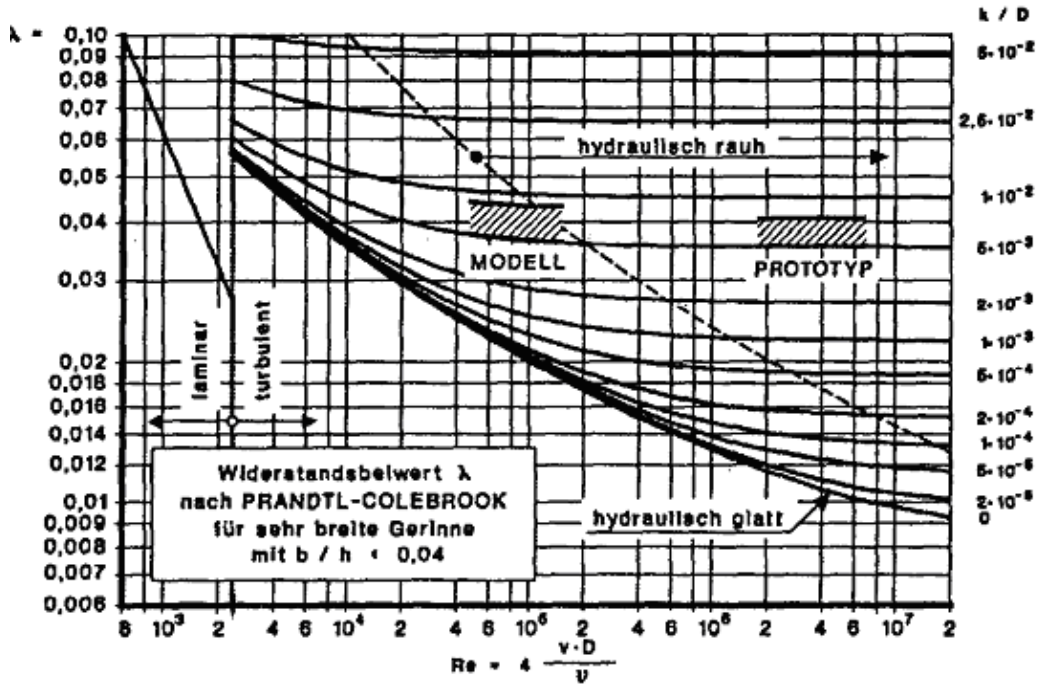

Figure 15: Friction factor against Reynolds numbers (Schulz, 1992)

20:1 and 40:1 with the structure and wave conditions being scaled according to the Froude law; in all cases the viscosity will be held constant. After discussions with the leader of work package 7 (Conclusions on scale effects and new data) it was agreed that a rough impermeable slope would be tested as well to determine whether the differences we expect to observe, theoretically, occurred in this case as well. For the impermeable case only one scale factor would be sufficient.

Following these discussions the AMAZON-SC code has been applied to the rough impermeable structure shown in Figure 16 at scales of 1:1 and 2:1 under regular waves ($T = 2$s, $H = 0.16$m at model. i.e. 1:1, scale). The numerical simulations have been performed over a period of ten seconds at model (1:1) scale during which time three waves over-top the sea wall. A numerical overtopping detector, located at the seaward edge of the crown, records both the instantaneous overtopping discharge per meter and the instantaneous jet velocity allowing the local jet Reynolds number (based on the characteristic length scale) to be computed. The measured velocity and overtopping discharge for 1:1 scale are shown in Figures 17 and 18, while Figures 19 and 20 show the results obtained at 2:1 scale (it should be noted that the wave period is $T = 2\sqrt{2}$ seconds in this case whilst the amplitude is 0.32 metres).

Based on the measured discharge the local, instantaneous, Reynolds number has been calculated (see Tables 3 and 4). A statistical analysis of these results shows that for scale 1:1 the Reynolds number lies between 5700 and 148500 with a median of 40500, while for scale 2:1 they Reynolds number lies between 13000 and 417000 with a median of 81500. These statistics are shown graphically in Figure 21. It is interesting to note that the minimum, maximum and median Reynolds numbers from the 2:1 case are slightly more than twice those observed in the 1:1 case. Figure 15 clearly shows that for nearly all roughnesses the results obtained from the 1:1 scale do not lie in the region where the friction factor may be considered independent of Reynolds number, while the large scale test the lower 50% of the observed Reynolds numbers are in this region. At larger scales it is likely that the friction factor will be independent of the Reynolds number for the majority of run-up and overtopping events.

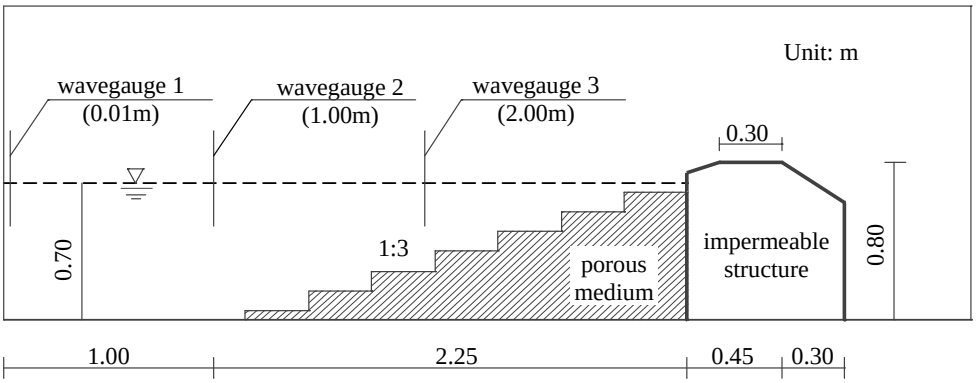

Figure 16: Regular roughness tests: general configuration at 1:1 scale.

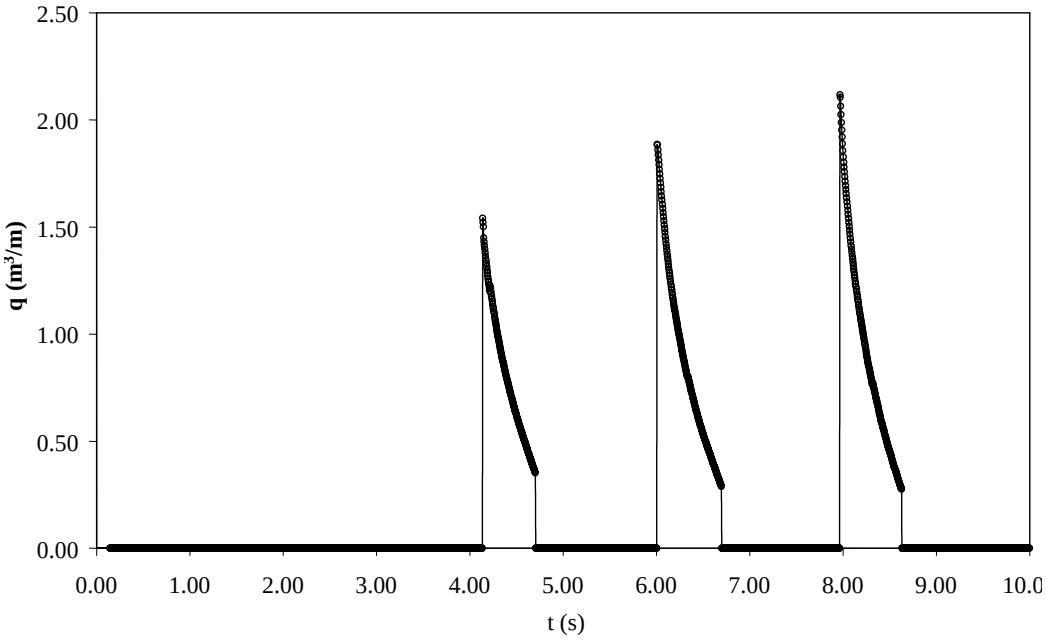

Figure 17: Regular roughness tests at 1:1 scale: Instantaneous discharge at the seaward edge of the crown.

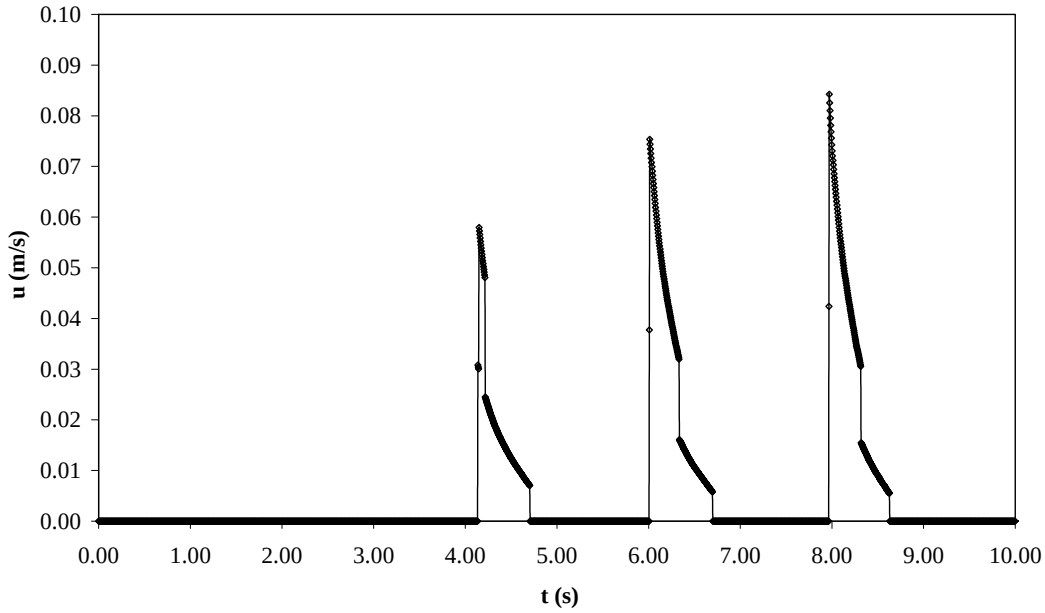

Figure 18: Regular roughness tests at 1:1 scale: Instantaneous velocity at the seaward edge of the crown.

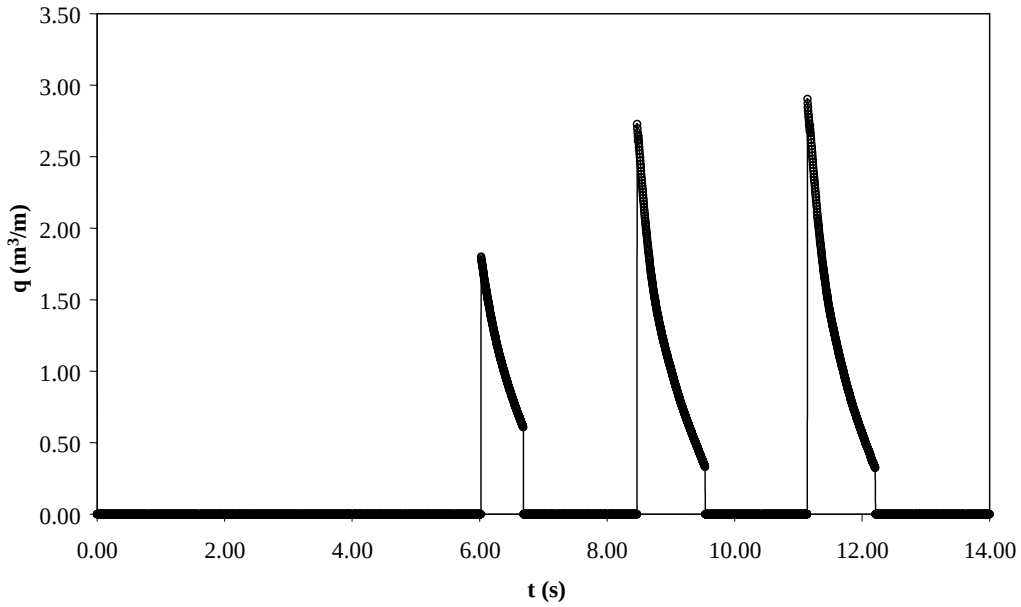

Figure 19: Regular roughness tests at 2:1 scale: Instantaneous discharge at the seaward edge of the crown.

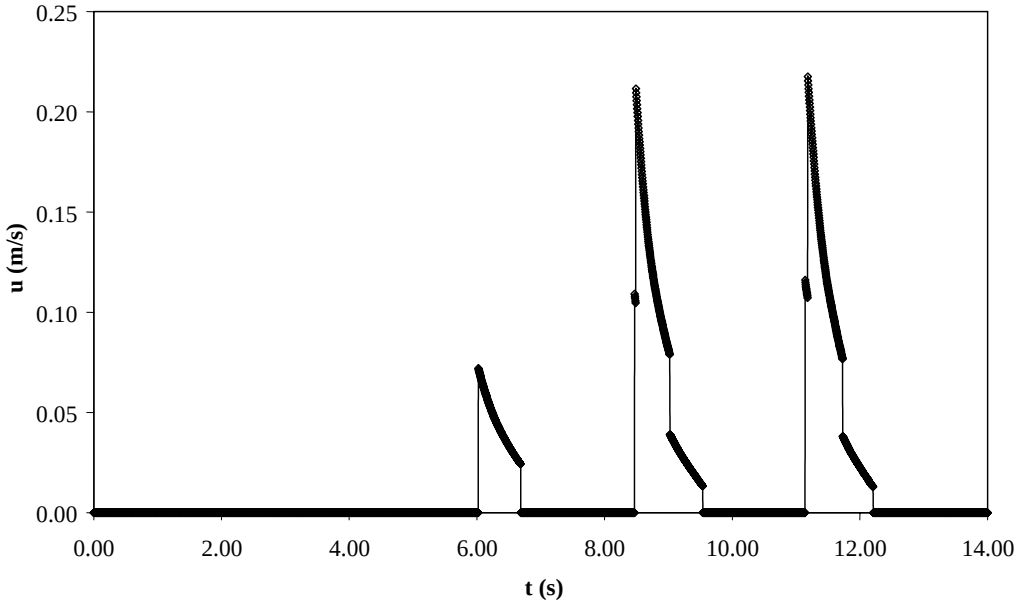

Figure 20: Regular roughness tests at 2:1 scale: Instantaneous velocity at the seaward edge of the crown.

The 1:1 scale factor case, presented in this analysis, is similar to the test conditions used in the small scale laboratory tests (in both flumes and basins) where the scaling factor from prototype is of the order of 1:40. The test clearly shows that for rough impermeable structures a laboratory scale of larger than 1:20 is required for the scale effects on friction factor to be negligible and for smoother structures this situation will be worse. The roughness length scale used in these tests is typical of armour layers with a 4m nominal diameter and for smoother structures the scale at which the tests need to be conducted must be larger as for smaller relative roughnesses the Reynolds number must be higher to archive hydraulic independence of the friction factor. The variation of the friction factor with time is shown in Figure 22.

Table 3: Instantaneous overtopping jet thickness and velocity for scale 1:1 measured at overtopping detector together with the derived instantaneous Reynolds number and friction factor.

	overtopping jet			friction
t(s)	thickness (m)	velocity (m/s)	Re	factor
4.2	0.06	1.2486	7.492E+04	0.125350
4.3	0.04	0.9960	3.984E+04	0.125516
4.4	0.04	0.7882	3.153E+04	0.125609
4.5	0.04	0.6216	2.486E+04	0.125729
4.6	0.02	0.4834	9.668E+03	0.126614
4.7	0.02	0.3546	7.092E+03	0.127137
6.0	0.06	1.8866	1.132E+05	0.125286
6.1	0.06	1.4480	8.688E+04	0.125324
6.2	0.04	1.1060	4.424E+04	0.125481
6.3	0.04	0.8682	3.473E+04	0.125568
6.4	0.04	0.6882	2.753E+04	0.125674
6.5	0.02	0.5354	1.071E+04	0.126474
6.6	0.02	0.4083	8.166E+03	0.126879
6.7	0.02	0.2885	5.770E+03	0.127585
8.0	0.08	1.8560	1.485E+05	0.125257
8.1	0.06	1.3640	8.184E+04	0.125334
8.2	0.04	1.0460	4.184E+04	0.125499
8.3	0.04	0.7982	3.193E+04	0.125603
8.4	0.02	0.6123	1.225E+04	0.126310
8.5	0.02	0.4526	9.052E+03	0.126713
8.6	0.02	0.3102	6.204E+03	0.127417

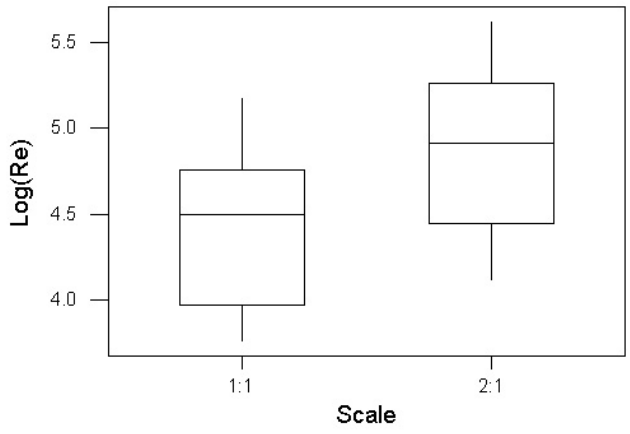

Figure 21: Boxplot of the $\log_{10}(Re)$ against scale for overtopping of a rough impermeable seawall.

Table 4: Instantaneous overtopping jet thickness and velocity for scale 2:1 measured at overtopping detector together with the derived instantaneous Reynolds number and friction factor.

	overtopping jet			friction
t(s)	thickness (m)	velocity (m/s)	Re	factor
6.0	0.12	1.8014	2.162E+05	0.125227
6.1	0.08	1.5820	1.266E+05	0.125273
6.2	0.08	1.3400	1.072E+05	0.125294
6.3	0.08	1.1380	9.104E+04	0.125317
6.4	0.04	0.9760	3.904E+04	0.125523
6.5	0.04	0.8330	3.332E+04	0.125585
6.6	0.04	0.7050	2.820E+04	0.125662
8.5	0.16	2.5900	4.144E+05	0.125196
8.6	0.12	2.0500	2.460E+05	0.125219
8.7	0.12	1.6515	1.982E+05	0.125233
8.8	0.08	1.3806	1.105E+05	0.125290
8.9	0.08	1.1836	9.469E+04	0.125311
9.0	0.08	1.1080	8.144E+04	0.125335
9.1	0.04	0.8612	3.445E+04	0.125571
9.2	0.04	0.7242	2.897E+04	0.125649
9.3	0.04	0.6008	2.403E+04	0.125748
9.4	0.04	0.4852	1.941E+04	0.125888
9.5	0.04	0.3732	1.493E+04	0.126104
11.2	0.16	2.6120	4.179E+05	0.125196
11.3	0.16	2.0913	3.346E+05	0.125204
11.4	0.12	1.6922	2.031E+05	0.125231
11.5	0.12	1.4029	1.684E+05	0.125245
11.6	0.08	1.1947	9.558E+04	0.125309
11.7	0.08	1.0078	8.062E+04	0.125337
11.8	0.08	0.8400	6.720E+04	0.125372
11.9	0.04	0.6948	2.779E+04	0.125669
12.0	0.04	0.5671	2.268E+04	0.125783
12.1	0.04	0.4482	1.793E+04	0.125947
12.2	0.04	0.3294	1.318E+04	0.126229

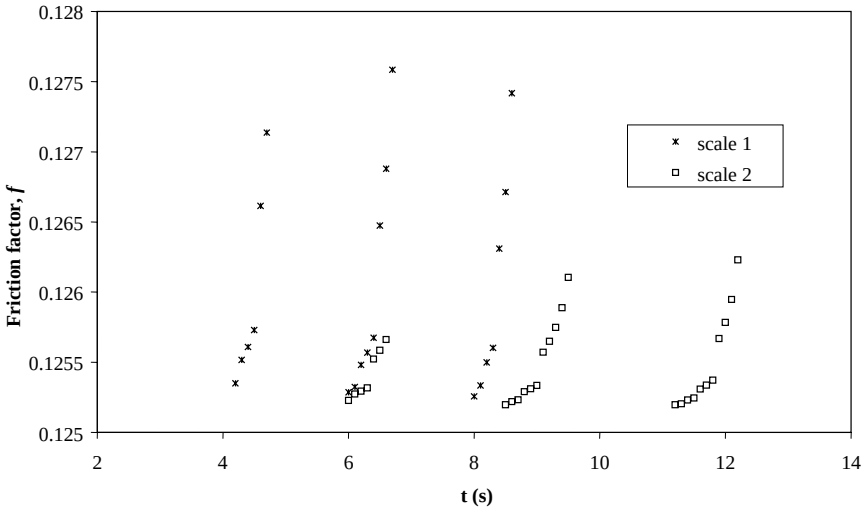

Figure 22: Instantaneous friction factor against time for overtopping events at both 1:1 and 2:1 scales.

4 UGent: LVOF

4.1 VoF Method and its Development

The VoF method is one of the most popular schemes used for free surface flows and has an established track record [10, 11, 12, 13, 14]. The mass conservation is its intrinsic feature. Additionally, it does not require special procedures to model topological changes of the front. On a stationary grid, one tracks the volume of each material in cells that contain a portion of an interface. The volume fractions (denoted as α hereafter) at mixed cells satisfy $0 < \alpha < 1$, in which the value of $\alpha = \frac{1}{2}$ is supposed to represent interfaces. Just the data α are specified, dependent on the shape and location of an initial interface. An iterative course of α involves a two-stage process: (i) an interface reconstruction algorithm; (ii) and an advection algorithm for α.

4.1.1 An interface reconstruction algorithm

Typically, an interface reconstruction algorithm is classified in two basic categories: explicit or implicit interface reconstructions. For the former, the current many approaches [15] are to describe an approximate interface (i.e., an Eulerian representation) according to the distributions of α. They are called the modern PLIC (piecewise linear interface calculation) methods. Clearly, it is more exact approximation to the interfaces once various possible orientations of the interface are predefined well [64, 10]. Alternative is to move the PLIC-type interfaces by virtue of a local velocity at a certain cell face. This type is sometimes called a Lagrangian interface reconstruction method according to a Lagrangian sense. During each single fractional step, the stretching or compression of the interface can be taken into account naturally [65]. This provides a more robust approach than the Eulerian reconstruction algorithm. For the latter, one assigns a piecewise-constant representation of the interface (e.g., the original Hirt and Nichols's VoF method [11]. This allows that interfaces are arbitrarily orientated with respect to the computational grid. Also, it is referred to as a purely Eulerian representation.

4.1.2 An advection algorithm

For an advection algorithm for α, one has to resolve the following transport equation:

$$\frac{\partial \alpha}{\partial t} + \frac{\partial (u\alpha)}{\partial x} + \frac{\partial (v\alpha)}{\partial y} + \frac{\partial (w\alpha)}{\partial z} = 0 \tag{26}$$

provided that the underlying velocity field and the reconstructed interface are given. Since α is a scalar quantity carrying the material information, Eq. (26) updates the values of α over mixed cells but maintains $\alpha = 1$ or 0 in the water or air, respectively. With an explicit interface reconstruction, it is relatively straightforward in its implementation for evaluation of the convective fluxes of α, based on the geometrical information from the reconstructed interface. Owing to without diffusion of the front, such approach [15] can give much better results than the original VoF method but at the cost of algorithmic complexity. In 3D situations, the operations to be performed could be more complicated in the context of mergers and breakups, in comparison to purely Eulerian methods [16]. On the other hand, with implicit interface reconstruction in the VoF methods, the critical issue is to discretise the convective terms. For solution of hyperbolic non-linear partial differential equation (PDE) of α (see Eq. 26), however, the problems are that the use of regular high-resolution schemes tends to be more or less diffusive for α over a few cells. Because of excessive diffusion [66, 67], non-physical deformation of the interface shape is observed [12], even using the very popular original VoF method (due to its simplicity). Some reasons may be interpreted as follows: it does not preserve local boundedness [13]. One approach to avoid such problems is to introduce a high resolution method with bounding treatments,

named the CICSM (compressive interface capturing scheme for arbitrary meshes) [13]. The relevant study can be found in Rudman [67] and Xiao [68], respectively.

4.2 The Present Work

In the current study, we developed a new solver [19] for modelling of wave run-up and wave overtopping events using a VoF method. Also, the code is capable of simulating the breaking of the periodical wave trains on the slope of a sea dike. Based on a split-implicit time differencing scheme, the Navier-Stokes equations filtered spatially are resolved over a Cartesian cut-cell mesh using a cell-staggered finite volume (FV) method, while incompressibility is enforced through an iterative Poisson solver for the pressure. The free surface is tracked using a VoF method that is simple enough to solve practical problems but still general enough to describe the physical behaviour, such as application in topologically complex interfacial flows. To realize this, the key is to develop an implicit process, i.e., without the knowledge of detailed interface information at each iteration, instead of an explicit process above mentioned. Consequently, the pressure and surface tension over mixed cells are treated implicitly. This allows to significantly simplify the application of the normal dynamic free surface boundary condition. In this way, the pressure at mixed cells is incorporated into the corresponding field equation, while the surface tension effects are modelled as a body force. Furthermore, no explicit expression for interface reconstruction is required during tracking, which is similar to the level set method widely applied to many fields. As expected, it can be generalized well to three dimensions (3D) and used for several industrial application as well. Our work in this area is to develop an approach which preserves both the smoothness of the interface and its sharp definition over one cell, indicating that numerical diffusion related with an upwind scheme should not be excessive (that is, without dispersing or wrinkling). It is composed of a weighted upwind scheme with the help of an operator-split second-order explicit Adams-Bashforth advection algorithm plus one high resolution scheme. When it is applied to test cases of complex flows caused by waves, our computation demonstrates that an approach proposed is simple and computationally efficient. The current study consists of the following numerical aspects:

- **LES;**
- **A fully implicit cell-staggered FV approach with a cut-cell Cartesian technique**;
- **A novel VoF solution**;
- **A blend of second- and fourth-order artificial damping terms**;
- **An absorbing-generating boundary condition for a wave generator**.

This is applied to:

- **to study the wave overtopping over coastal structures**
- **to study the effect of current on breaking wave-structure interactions**;
- **to investigate the effects of viscosity on the wave boundary layer**;
- **to estimate wave impacts**;
- and **3D effects**.

This section of the report is organized as follows. First, we briefly describe our numerical methods that include the mathematical models, the initial and boundary conditions and numerical treatment. The calculated results and discussions, such as the convergence

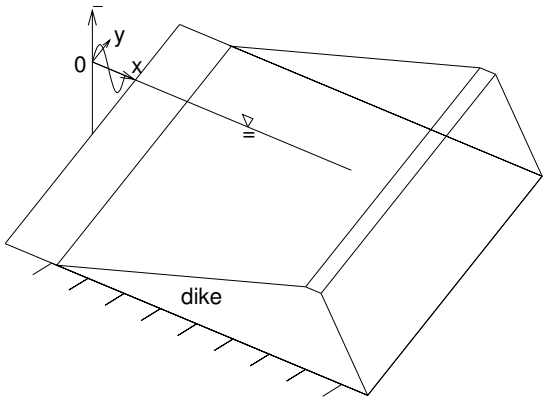

Figure 23: A reference coordinate system for sea dike problems.

performance, the study of the grid refinement effects, the influences of current and the Reynolds stress on the wave-induced motions and the wave-boundary layer, respectively, plus a comparison with measurements available, are presented next, followed by some concluding remarks.

4.3 Our Numerical Methods

4.3.1 A LES Model

A reference coordinate system for sea dike problems, for example, is illustrated in Fig. 23, where the origin is fixed at the intersection of the inlet with the still water line, x is in the direction of the wave propagation, y and z are positive toward the width of a dike and upwards, respectively.

By convoluting, the governing equations for the large-scale eddies are expressed as

$$\frac{\partial \overline{\varphi}}{\partial t} + \frac{\partial \overline{F}}{\partial x} + \frac{\partial \overline{G}}{\partial y} + \frac{\partial \overline{H}}{\partial z} = \overline{Q} \tag{27}$$

according to the predefined filter kernel. The variables $\overline{\varphi} = (0,\ \overline{u},\ \overline{v}\ ,\overline{w})^T$. $\overline{F} = \overline{F}_i - \overline{F}_v + \overline{F}_a,\ \overline{G} = \overline{G}_i - \overline{G}_v + \overline{G}_a$ and $\overline{H} = \overline{H}_i - \overline{H}_v + \overline{H}_a$, in which the inviscid fluxes $(\overline{F}_i,\ \overline{G}_i,\ \overline{H}_i)$, the viscous fluxes $(\overline{F}_v,\ \overline{G}_v,\ \overline{H}_v)$, the acoustic fluxes $(\overline{F}_a,\ \overline{G}_a,\ \overline{H}_a)$ and the source term $(\overline{Q})$ represent, respectively

$$\overline{F}_i = \begin{pmatrix} 0 \\ \overline{u}^2 \\ \overline{v}\ \overline{u} \\ \overline{w}\ \overline{u} \end{pmatrix}, \overline{G}_i = \begin{pmatrix} 0 \\ \overline{u}\ \overline{v} \\ \overline{v}^2 \\ \overline{w}\ \overline{v} \end{pmatrix}, \overline{H}_i = \begin{pmatrix} 0 \\ \overline{u}\ \overline{w} \\ \overline{v}\ \overline{w} \\ \overline{w}^2 \end{pmatrix}.$$

$$\overline{F}_v = \begin{pmatrix} 0 \\ \overline{\nu}_e \frac{\partial \overline{u}}{\partial x} \\ \overline{\nu}_e \frac{\partial \overline{v}}{\partial x} \\ \overline{\nu}_e \frac{\partial \overline{w}}{\partial x} \end{pmatrix}, \overline{G}_v = \begin{pmatrix} 0 \\ \overline{\nu}_e \frac{\partial \overline{u}}{\partial y} \\ \overline{\nu}_e \frac{\partial \overline{v}}{\partial y} \\ \overline{\nu}_e \frac{\partial \overline{w}}{\partial y} \end{pmatrix}, \overline{H}_v = \begin{pmatrix} 0 \\ \overline{\nu}_e \frac{\partial \overline{u}}{\partial z} \\ \overline{\nu}_e \frac{\partial \overline{v}}{\partial z} \\ \overline{\nu}_e \frac{\partial \overline{w}}{\partial z} \end{pmatrix}.$$

$$\overline{F}_a = \begin{pmatrix} \overline{u} \\ \frac{1}{\overline{\rho}} \overline{p} \\ 0 \\ 0 \end{pmatrix}, \overline{G}_a = \begin{pmatrix} \overline{v} \\ 0 \\ \frac{1}{\overline{\rho}} \overline{p} \\ 0 \end{pmatrix}, \overline{H}_a = \begin{pmatrix} \overline{w} \\ 0 \\ 0 \\ \frac{1}{\overline{\rho}} \overline{p} \end{pmatrix}.$$

with $\overline{Q} = (0,\ \frac{1}{\overline{\rho}}\overline{F}_b^x,\ \frac{1}{\overline{\rho}}\overline{F}_b^y,\ \frac{1}{\overline{\rho}}\overline{F}_b^z - g)^T$. $(\overline{u},\ \overline{v},\ \overline{w})$ are the components of the velocity in the $x-$, $y-$ and $z-$directions, respectively, $\overline{p}$ is the total pressure, and g is the gravitational acceleration. $(\overline{F}_b^x,\ \overline{F}_b^y,\ \overline{F}_b^z)$ are three components of a body force $\mathbf{F}_b$ in the $(x,\ y,\ z)$-directions, respectively, which are modelled according to the continuous surface force (CSF) manner [69]. $\overline{\nu}_e = \nu + \overline{\nu}_t$ is the effective viscous coefficient, in which ν is the molecular viscosity and $\overline{\nu}_t$ is the eddy viscosity to be determined with a turbulence model. The local density $\overline{\rho}$ and viscosity $\overline{\nu}_e$ are given as in terms of $\overline{\alpha}$ in the volume-of-fluid (VoF)

$$\overline{\rho} = \overline{\alpha}\ \overline{\rho}_w + (1-\overline{\alpha})\,\overline{\rho}_a, \quad \overline{\nu}_e = \overline{\alpha}\ \overline{\nu}_{e_w} + (1-\overline{\alpha})\,\overline{\nu}_{e_a}$$

where the subscripts $(w,\ a)$ denote the water and air, respectively. The solution of the volume fractions $\overline{\alpha}$ is based on the transport equation as follows:

$$\frac{\partial\overline{\alpha}}{\partial t} + \frac{\partial(\overline{u}\ \overline{\alpha})}{\partial x} + \frac{\partial(\overline{v}\ \overline{\alpha})}{\partial y} + \frac{\partial(\overline{w}\ \overline{\alpha})}{\partial z} = \overline{\alpha}\left\{\frac{\partial\overline{u}}{\partial x} + \frac{\partial\overline{v}}{\partial y} + \frac{\partial\overline{w}}{\partial z}\right\} \tag{28}$$

instead of Eq. (26).

4.3.2 Solution Procedures

Discretisation of the conservation of Eq. (27) may be realized with a cell-staggered FV method on non-uniform cut-cell grids. By integrating, application of Gauss's divergence theorem to the divergence of the differential form yields

$$\frac{\partial}{\partial t}\int_V \overline{\varphi}dV + \int_S \overline{\mathbf{F}}\cdot d\mathbf{S} = \int_V \overline{Q}dV \tag{29}$$

for the surface S surrounding the domain of interest V. Accordingly, the discretisation of Eq. (29) over each cell of a hexahedron at the $(n+1)$th time level is driven by

$$\frac{\partial\overline{\varphi}^{n+1}}{\partial t} = -\frac{1}{V}\sum_{faces}\widehat{\overline{\mathbf{F}}}^{n+1}S + \overline{Q}^{n+1} \tag{30}$$

The subscript $faces$ represents the summation over all cell faces of the computational cell. $\widehat{\overline{\mathbf{F}}}$ includes the inviscid, viscous and acoustic fluxes via

$$\begin{aligned}\widehat{\overline{\mathbf{F}}} &= n_x\left(\overline{F}_i - \overline{F}_v + \overline{F}_a\right) + n_y\left(\overline{G}_i - \overline{G}_v + \overline{G}_a\right)\\ &+ n_z\left(\overline{H}_i - \overline{H}_v + \overline{H}_a\right)\end{aligned}$$

where (n_x, n_y, n_z) are three unit outward surface normal components in the $x-, y-$ and $z-$directions, respectively.

By introducing $\delta\overline{\varphi} = \overline{\varphi}^{n+1} - \overline{\varphi}^n$ for the velocity, and enforcing a local linearisation of the fluxes in time t: $\widehat{\overline{\mathbf{F}}}^{n+1} = \widehat{\overline{\mathbf{F}}}^n + \frac{\partial\widehat{\overline{\mathbf{F}}}}{\partial\varphi}\delta\overline{\varphi}$, only for the convective and diffusion terms, thus Eq. (30) can be factored into the following three one-dimensional equations:

$$\begin{aligned}-\overline{A}_{i-1}\delta\overline{\varphi}^{**}_{i-1} + \overline{A}_p^{(1)}\delta\overline{\varphi}^{**} - \overline{A}_{i+1}\delta\overline{\varphi}^{**}_{i+1} &= \Delta t\overline{R}\\ -\overline{A}_{j-1}\delta\overline{\varphi}^{*}_{j-1} + \overline{A}_p^{(2)}\delta\overline{\varphi}^{*} - \overline{A}_{j+1}\delta\overline{\varphi}^{*}_{j+1} &= \delta\overline{\varphi}^{**}\\ -\overline{A}_{k-1}\delta\overline{\varphi}_{k-1} + \overline{A}_p^{(3)}\delta\overline{\varphi} - \overline{A}_{k+1}\delta\overline{\varphi}_{k+1} &= \delta\overline{\varphi}^{*}\end{aligned} \tag{31}$$

based on the alternative directional implicit (ADI) approximate factorization with a local time step Δt. Three mainly diagonal coefficients $\overline{A}_p^{(1)}, \overline{A}_p^{(2)}$ and $\overline{A}_p^{(3)}$ are, respectively,

$$\begin{aligned}\overline{A}_p^{(1)} &= 1 + \overline{A}_{i+1} + \overline{A}_{i-1} + \frac{\Delta t}{V}\left(\dot{\overline{M}}_{i+\frac{1}{2}} - \dot{\overline{M}}_{i-\frac{1}{2}}\right)\\ \overline{A}_p^{(2)} &= 1 + \overline{A}_{j+1} + \overline{A}_{j-1} + \frac{\Delta t}{V}\left(\dot{\overline{M}}_{j+\frac{1}{2}} - \dot{\overline{M}}_{j-\frac{1}{2}}\right)\\ \overline{A}_p^{(3)} &= 1 + \overline{A}_{k+1} + \overline{A}_{k-1} + \frac{\Delta t}{V}\left(\dot{\overline{M}}_{k+\frac{1}{2}} - \dot{\overline{M}}_{k-\frac{1}{2}}\right)\end{aligned}$$

The coefficients ($\overline{A}_{i\pm1},\ \overline{A}_{j\pm1},\ \overline{A}_{k\pm1}$) typically involve a blend of the inviscid volumetric fluxes with the viscous ones, which can be obtained with an one-order upwind scheme for the former and a central difference scheme for the latter, as evaluating the corresponding derivatives $\frac{\partial\widehat{\overline{\mathbf{F}}}}{\partial\varphi}$ at a certain face. $\overline{A}_{i+1}$, for example, is given by

$$\overline{A}_{i+1} = \frac{\Delta t}{V}\left(\dot{\overline{M}}^{-}_{i+\frac{1}{2}} + \overline{K}_{i+\frac{1}{2}}\right)$$

with

$$\dot{\overline{M}}^{-}_{i+\frac{1}{2}} = max\left(-\dot{\overline{M}}_{i+\frac{1}{2}}, 0\right) = max\left\{-\left(\overline{u}_n S\right)_{i+\frac{1}{2}}, 0\right\},$$
$$\overline{K}_{i+\frac{1}{2}} = \left(\frac{\overline{\nu}_e S}{\Delta x}\right)_{i+\frac{1}{2}}.$$

Similar definition is for $\overline{A}_{j\pm1}$ and $\overline{A}_{k\pm1}$ by index substitution. $\overline{R}$ is the residual of the momentum equations defined as

$$\overline{R} = -\left\{\frac{1}{V}\sum_{faces}\left(\overline{F}^n_i - \overline{F}^n_v\right) - \overline{Q}^n\right\}$$

where the source terms, $\overline{Q}^{n+1} = \overline{Q}^n = (0,\ 0,\ 0,\ -g)^T$.

Given the explicit inviscid and viscid fluxes, $\delta\overline{\varphi}$ can be achieved. In our study, the former is achieved by means of the flux-difference splitting approach, while the corresponding face values are estimated with a second-order essentially non-oscillatory (ENO) scheme [2]; the latter is easy to obtain with a central-difference scheme.

Under the surface tension effects, a temporal velocity $\tilde{\overline{\varphi}}$ is renewed by

$$\tilde{\overline{\varphi}} = \overline{\varphi}^n + \delta\overline{\varphi} + \frac{1}{\overline{\rho}}\overline{F}^i_b \tag{32}$$

which can be used for achievement of the pressure with a projected algorithm. Using an implicit three-level second-order scheme for the time derivative, the final velocity is given by

$$\overline{\varphi}^{n+1} = \frac{2}{3}\left(\overline{\varphi}^n - \frac{1}{2}\overline{\varphi}^{n-1} + \tilde{\overline{\varphi}} - \frac{\Delta t}{\overline{\rho}}\frac{\partial\overline{p}}{\partial x_i}\right) \tag{33}$$

provided that the pressure from the Poisson solver is available. The superscripts ($n-1,\ n,\ n+1$) stand for the previous, current and next time levels, respectively.

For solution of a step profile of $\overline{\alpha}$ in VoF, a hybrid approach [19] that includes the weighted upwind scheme and a blending one is adopted, dependent of the distributions of $\overline{\alpha}$. This is a simple and effective approach, especially without the need of interface reconstruction during tracking. When neighbours of a cell (i) become an empty cell having $\overline{\alpha} = 0$, for example, the blending scheme will be activated. Otherwise, the weighted upwind one is active, indicating that $\overline{\alpha}_{i+\frac{1}{2}}$ at $(i+\frac{1}{2})$ face in the coordinate direction of x is updated by ($\dot{\overline{M}}_{i+\frac{1}{2}} \geq 0$ in this case)

$$\overline{\alpha}_{i+\frac{1}{2}} = \Gamma\overline{\alpha}^n_i + (1-\Gamma)\left(-\overline{\alpha}^L_{i+\frac{1}{2}}\right) \tag{34}$$

when $\overline{\alpha}^n_{i-1}$ or $\overline{\alpha}^n_{i+1} \neq 0$. The subscripts $(i-1, i+1)$ represent two neighbours of cell (i), respectively, and the face $(i+\frac{1}{2})$ lies between cells (i) and $(i+1)$. Owing to enforcing a compressive discretization, the value at the face $(i+\frac{1}{2})$ always takes its left state, $\overline{\alpha}^L_{i+\frac{1}{2}}$, which can be evaluated with the ENO scheme. Namely

$$\overline{\alpha}^L_{i+\frac{1}{2}} \quad = \quad \overline{\alpha}_i + \frac{1}{2}m\left(\overline{\alpha}_{i+1} - \overline{\alpha}_i, \overline{\alpha}_i - \overline{\alpha}_{i-1}\right)$$

with the function $m(a,b)$ defined as

$$m(a,b) = \begin{cases} a, & \text{if } \mid a \mid \leq \mid b \mid; \\ b, & \text{otherwise.} \end{cases}$$

Γ represents a flux-limiter determined by introduction of van Leer's monotone algorithm [70]

To suppress oscillations in regions of a strong pressure gradient, a blend of second- and fourth-order artificial damping terms is designed for correction of the normal face velocity $\overline{u}_n$, because of its high-frequency damping capability. At the inlet, an absorbing-generating boundary condition is introduced so that a well-suited boundary value for $\overline{\alpha}$ is specified. The more detailed description can be found in our current paper[19].

4.3.3 Initial and Boundary Conditions

Initial conditions

All simulations started from complete rest via $\overline{u} = \overline{v} = \overline{w} = 0$ at $t = 0$. According to a flat free surface, the volume fractions $\overline{\alpha}$ are initially assigned by (with respect to the still water line)

$$\overline{\alpha} = \begin{cases} 1, & \text{in the fluid;} \\ \overline{\alpha}, & \text{over mixed cells;} \\ 0, & \text{in a void.} \end{cases}$$

Boundary conditions

The bottom effect is incorporated by enforcing the slip boundary conditions for a cut cell, while the no-slip boundary conditions are applied in the lateral direction. At an interface (defined by a free surface) between the water and air, the contribution from the air is only to apply the pressure on the water. Since surface tension is handled as a body force, consequently, the normal dynamic free surface boundary condition is approximated with $\overline{p} = 0$. In this case, the condition of $\overline{p} = 0$ is satisfied by setting the corresponding coefficient to zero in the matrix of the pressure Poisson equation. Such a treatment is to avoid the need for the extrapolated pressure over mixed cells. At the inlet, an absorbing-generating boundary condition is applied, while the following Orlanski's open boundary condition is employed at the outlet:

$$\frac{\partial \overline{\beta}}{\partial t} + c\frac{\partial \overline{\beta}}{\partial x} = 0$$

which helps to dissipate the energy of outgoing waves. $\overline{\beta} = (\overline{u},\ \overline{v},\ \overline{w},\ \overline{\alpha})$. c is the phase velocity of the wave train and $c = \sqrt{gd}$ with a finite water depth d.

An absorbing-generating boundary condition

Based on the assumption of the linear waves, the total waves (φ_t) are related to the incident waves (φ_i) via the reflected waves $\varphi_r = \varphi_t - \varphi_i$. Thus, one has

$$\frac{\partial \varphi_t}{\partial t} - c\frac{\partial \varphi_t}{\partial x} = \frac{\partial \varphi_i}{\partial t} - c\frac{\partial \varphi_i}{\partial x} \tag{35}$$

Which forms the so-called absorbing-generating boundary condition for a wave generator fixed at the inlet. According to the linear wave theory, the evaluation of the source terms in

the right hand of Eq. (35) is straightforward for regular waves, once the three components (u, v, w) of the velocity at one ghost cell are given by

$$\begin{aligned} u &= u_c + \frac{H}{2}\left(\omega_a - k u_c\right)\frac{cosh\left\{k\left(z+d\right)\right\}}{sinh\left(kd\right)} cos\left\{k\left(x+\frac{\lambda}{4}\right) - \omega_a t\right\} \\ v &= 0 \\ w &= \frac{H}{2}\left(\omega_a - k u_c\right)\frac{sinh\left\{k\left(z+d\right)\right\}}{sinh\left(kd\right)} sin\left\{k\left(x+\frac{\lambda}{4}\right) - \omega_a t\right\} \end{aligned} \tag{36}$$

where u_c is the steady vertically-uniform current specified in the INPUT file. In this case, two different current speeds u_c = 0.5 and -0.5 m/s are given, which correspond to the following- and opposing-current, respectively. Within the moving frame of reference, the wave orbital velocity u_w is related to the relative wave celerity u_r via the current velocity u_c. Thus, we have

$$u_r = u_w - u_c cos\beta \tag{37}$$

This leads to the absolute frequency ω_a as

$$\omega_a = \omega_r + k u_c cos\beta \tag{38}$$

with $\omega_r^2 = gk \cdot tanh(kd)$ and the wave number k defined by $k = 2\pi/\lambda$, where the wave length λ is determined by

$$\lambda = \left\{\left[\frac{g\lambda}{2\pi} tanh\frac{2\pi d}{\lambda}\right]^{\frac{1}{2}} + u_c cos\beta\right\} T_a \tag{39}$$

based on a Newton-Raphson technique. T_a is the apparent wave period. In this study, waves propagate into a current without obliqueness, indicating that an angle β to the wave orthogonal is set to zero. Consequently, two cases can be taken into account as follows:

- wave-following-current conditions;
- wave-opposing-current conditions.

Clearly, a pure wave can be easily generated in the inlet, provided that u_c=0 is enforced. On the other hand, a pure flow can be also obtained without the presence of a linear wave.

4.4 Test Cases

For validation of our numerical approach, two test cases associated with overtopping of waves are selected, which are well known design problems in coastal and harbour engineering. Both cases involve breaking surface waves during overtopping. Flows are driven by a wave generator for regular and irregular waves, located at the inlet. For the former, for example, the amplitude (H = 0.16 m) and period (T = 2 s) plus the water depth (d = 0.7 s), are given, while the latter is created by superimposing a series of regular waves. Computations are conducted in a numerical flume, where a typical computational domain overlapping the dike (or the barrier) consists of a total length of 6.3 m and a height of 1 m (see Fig. 24 for a Cartesian cut-cell mesh, generated by cutting the dike out of a background Cartesian mesh). Note that in this report we shall present our results for a smooth impermeable sea dike. Another case (over a vertical fixed barrier in the front of a pier) can be found in our current study [19, 71]. The calculated results are represented in terms of the wave-induced velocity fields and the time history of the surface elevation $\overline{\eta}$ (m) at certain points. The calculated pressure is nondimensional with the density (ρ), water depth (d) and gravitational acceleration (g). According to an usual tradition, x = 0 and 6.3 m denote the inlet and outlet, respectively.

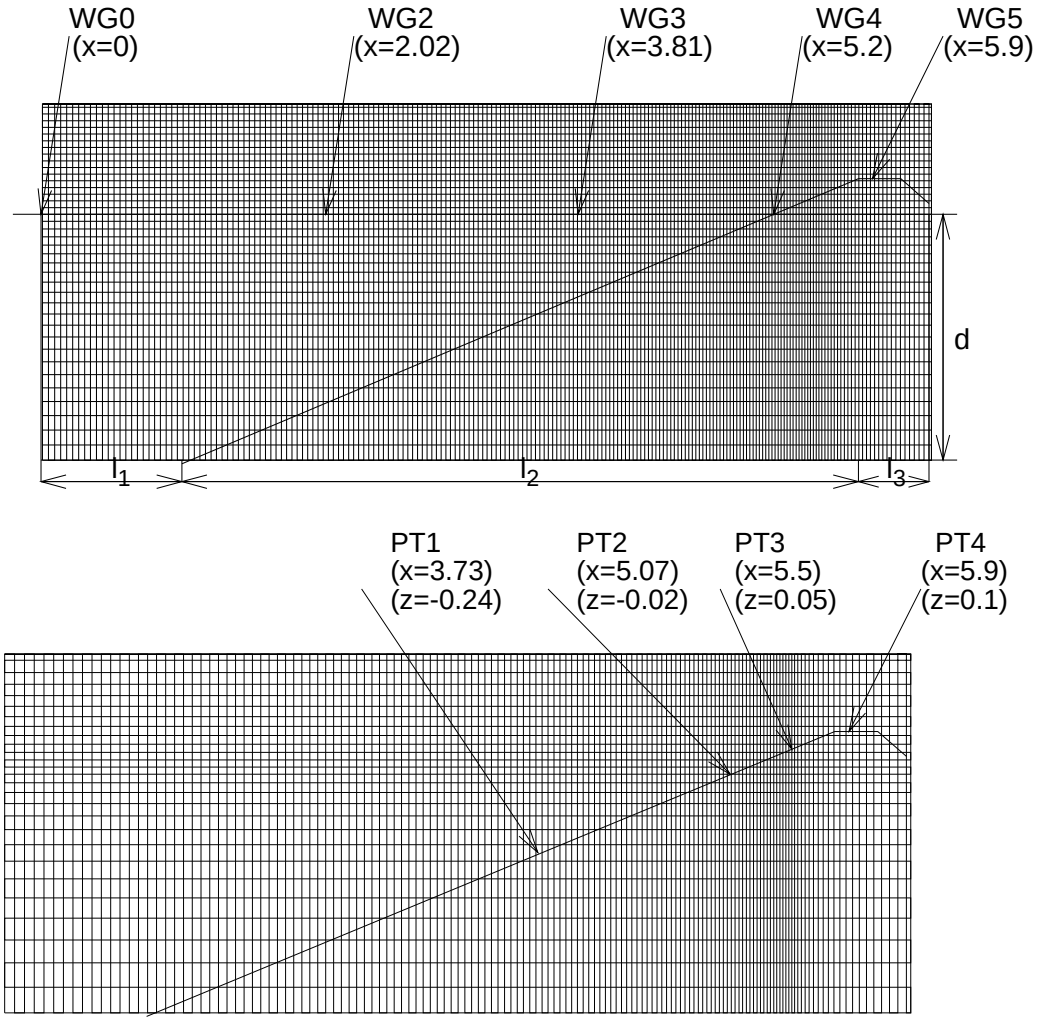

Figure 24: Computational domain on a non-uniform Cartesian cut-cell mesh for sea dike problems. WG0 to WG5 represent five wave gauges (WG), and PT1 to PT4 stand for four pressure transducers (PT). l_1=1.0 m, $l_1 + l_2 + l_3$=6.3 m and d=0.7 m.

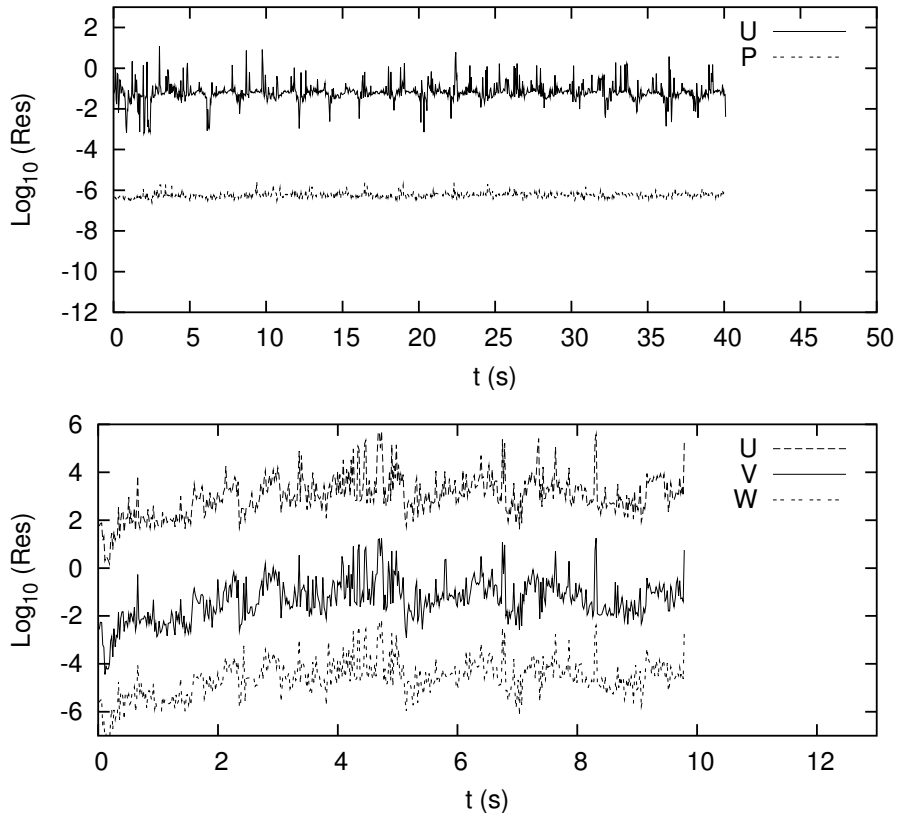

Figure 25: Convergence histories of the L_2 norm of the residuals (U, W, P) on grids 251×40 for both cases: the regular (top) and irregular (bottom) waves.

4.5 Calculated Results and Discussions

4.5.1 Convergence History

Our iterative convergence is assessed by examining the L_2 norm of the residuals (Res) for the momentum equation (U, W) in the $x-$ and z-directions and the pressure (P) on one mesh, as illustrated in Fig. 25 for the regular (top) and irregular (bottom) waves, respectively. As expected, the incomplete Cholesky conjugate gradient (ICCG) algorithm [72] achieves the fast convergence rates for the pressure due to the well preconditioning technique. The curves for both cases look the horizontal shape but oscillate within a certain region (around the value of -6), for example, as illustrated in Fig. 25). In our case, the excellent behaviour of convergence for the pressure implies that our simulations are stable even during lengthy computations. More importantly, it provides one measure for verifying the calculated results, because it is impossible to achieve good results without the convergence for the pressure. The behaviour for the velocity is less satisfactory than the pressure.

4.5.2 Grid Refinement Effects

Fig. 26 displays the effects of the grid density on the wave-induced motions with two grid levels. The fine grid with varying cell sizes is 251×40 in the $x-$ and $z-$directions, respectively, and the coarse one is 145×28. It is observed that more detailed physical phenomena of motions can be represented with increased mesh refinement, as shown in Fig. 26 for the wave-induced velocity fields at a given $t = 11.0$ s. Clearly, the coarse grid does not detect well motions due to insufficient grid resolution. But the flows tend to be more realistic as the mesh is refined. Interestingly, a regular shape of the wave profiles may be resolved

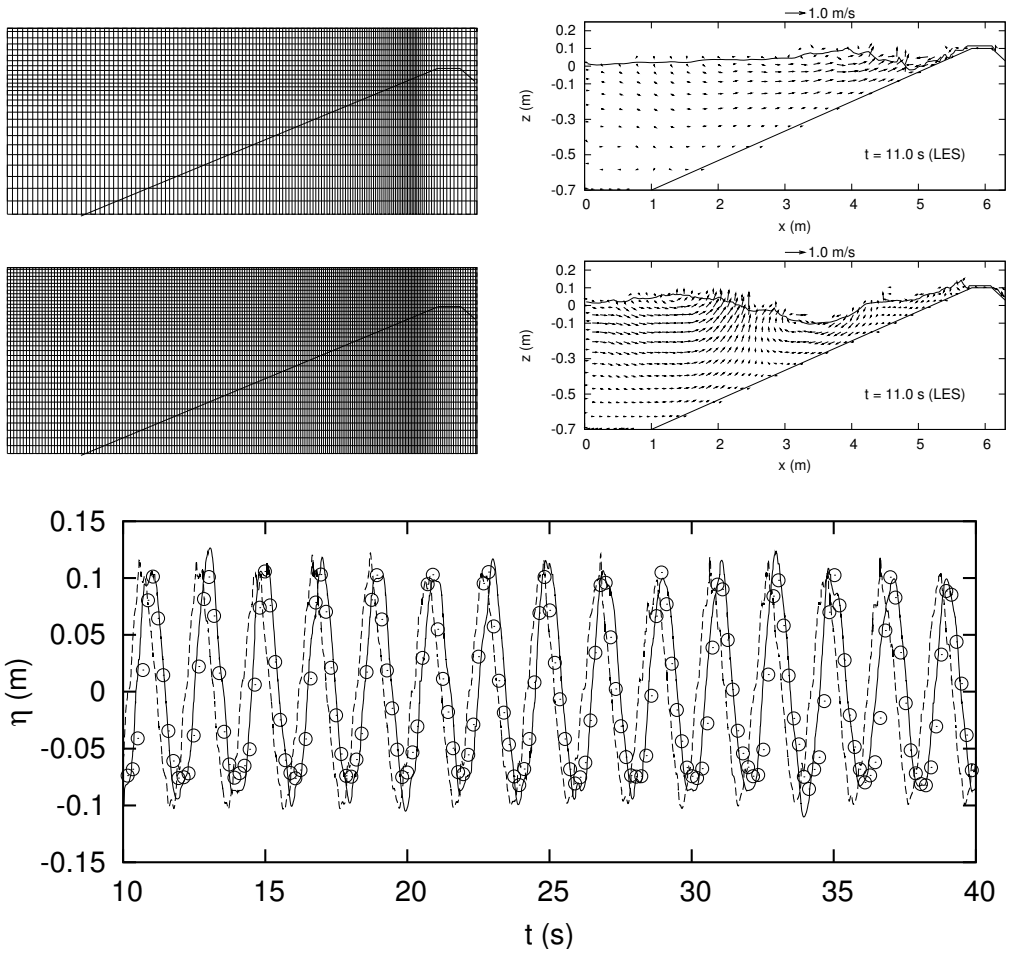

Figure 26: Grid refinement effects for the velocity fields induced by the irregular waves at a given time $t = 11.0\ s$ and the surface elevation (the regular waves) versus time at $WG2$ ($x = 2.02\ m$). —— 251×40; − − − 145×28; o Measurement.

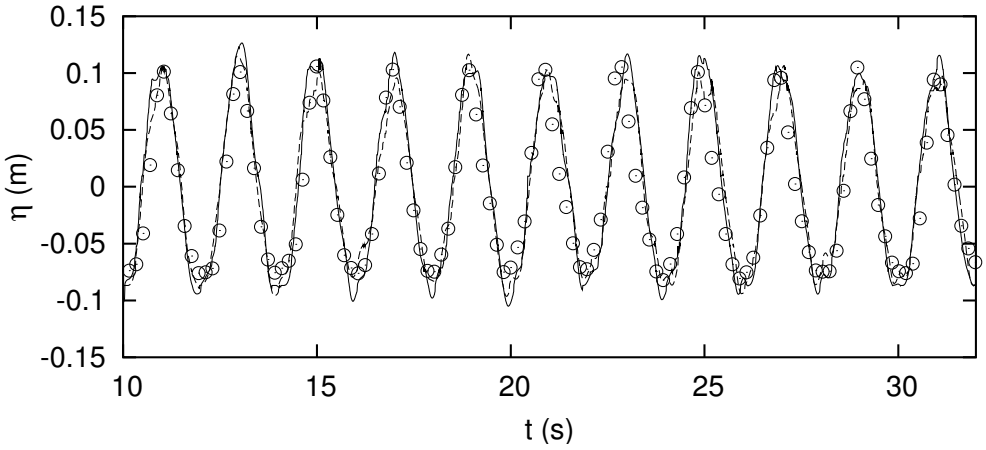

Figure 27: Comparison of a dynamic LES with a static one for the surface elevation versus time at one points ($x = 2.02$m). —— a dynamic LES; − − − a static LES; o Measurement.

adequately for both meshes (see Fig. 26 for the time trace of the surface elevation at one point, $x = 2.02$ m), indicating that differences attributed to the grid effects are relatively small for the surface elevation and mainly limited to the capture of fine structures for the velocity fields. Consequently, the current fine mesh (251×40) may be suited to capture most of the wave-induced motions so that the CPU time required does not cost much more for Linux based PC.

4.6 Comparison between a Dynamic and Static LES

Broadly, globally similar but only a little different local feature is apparent, as shown in Fig. 27, comparing a dynamic LES with a static one. Both models capture the overall shape of the wave profiles, which exhibits a feature of typical non-linearity: higher and narrower peak; and flatter troughs. All the results agree with the experimental data, whereas a slight improvement is achieved using a dynamic LES. Using a static Smagorinsky model, the eddy viscosity coefficient $\overline{\nu}_t$ is given by

$$\overline{\nu}_t = C_s \left(\overline{\Delta}\right)^2 |\overline{S}| \tag{40}$$

where C_s is Smagorinsky's constant. $\overline{\Delta}$ is a characteristic length scale of the small eddies, for example, in our case, $\overline{\Delta} = \min(\Delta x, \Delta y, \Delta z)$, and $|\overline{S}| = \sqrt{2\overline{S}_{ij}\overline{S}_{ij}}$ is the Frobenius norm of the rate strain tensor $\overline{S}_{ij}$. In the latter case, it is calculated by the vorticity components $|\overline{S}| = |\nabla \times \overline{\mathbf{V}}|$ with $\overline{\mathbf{V}} = \overline{u}\mathbf{i} + \overline{v}\mathbf{j} + \overline{w}\mathbf{k}$, instead of the velocity strain rate $\overline{S}_{ij}$.

The use of the dynamic procedure, on the other hand, is adaptively to evaluate adjustable parameter C_s (see Eq. 40) from the resolved scales. Consequently, it eliminates the uncertainty associated with the tunable model parameter in a static Smagorinsky model, indicating that this helps to correlate with varying in different regions of the flow. In this study, we follow the dynamic Smagorinsky's model due to its wide application. The emphasis in the application of a dynamic subgrid-scale model is given by our current paper [20], which is our extension to the paper [19], where most results are obtained based on a static Smagorinsky model.

4.6.1 Development of Waves at Dike Crest

Fig. 28 exhibits the surface elevation against time at one point of interest, that is, on the dike crest ($WG5$, $x = 5.9$ m) for the regular and irregular waves, respectively.

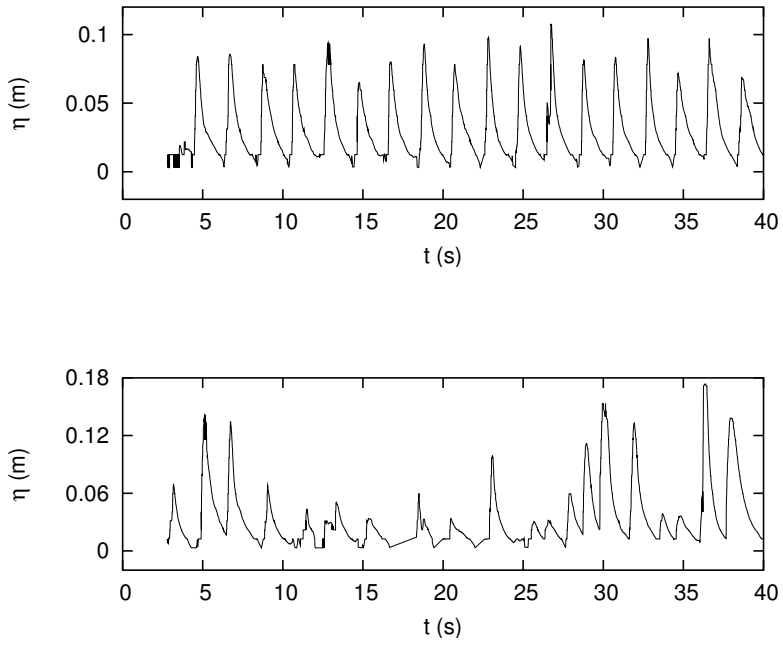

Figure 28: Time sequence of the surface elevation at one point, $WG5$, $x = 5.9$ m. Top: the regular waves; bottom: the irregular waves.

Typically, it directly records a signal from wave overtopping events so that useful information for design of the dike is provided like the layer thickness, the discharge and the cumulative overtopped volume of water. As expected, the desirable shape, which increases rapidly first and then diminishes slowly, as shown in Fig. 28, is reproduced.

4.6.2 Wave Impact: time signals of the pressure on the dike

A better understanding of the wave impact loading on the dike slope is illustrated in Fig. 29 for the time signals of the impact pressure on the slope at points PT1 to PT4 (see Fig. 24).

Except at PT1 (see Fig. 29 for the top, where the variation of the pressure is almost uniform), one can see that the pressure slowly drops after a sharp increase, which is similar as observed in the physical model. For example, the computations at PT4 (see Fig. 29 for the bottom) correspond to the change of the surface elevation (see Fig. 28: top).

4.6.3 Wave-Induced Velocity Fields at Several Stages

Fig. 30 illustrates the velocity fields at different time levels. This provides one observation of the wave-induced motions in the region of interest with several stages: the wave attack, run-up, run-down, waves breaking to overtopping of waves. As compared, motions caused by the irregular waves look more complex than those by the regular waves. Generally, as more waves pass over the dike crest, the flow becomes fully turbulent after an initial transient period so that the features of the flow pattern tend to be very complex, often subjected to the steepness of the free surface most likely associated with a cycle of splashing and the vortex formation created by the velocity. Waves continuously break, while the energy of waves is dissipated by turbulence and convected by vortices. At $t = 32.2$ s, the wave height increases as it shoals on the front face. By 32.4 s, a violent overtopping jet will occur again. Additionally, the corresponding motions display the down wash at $t = 33.2$ s, while the

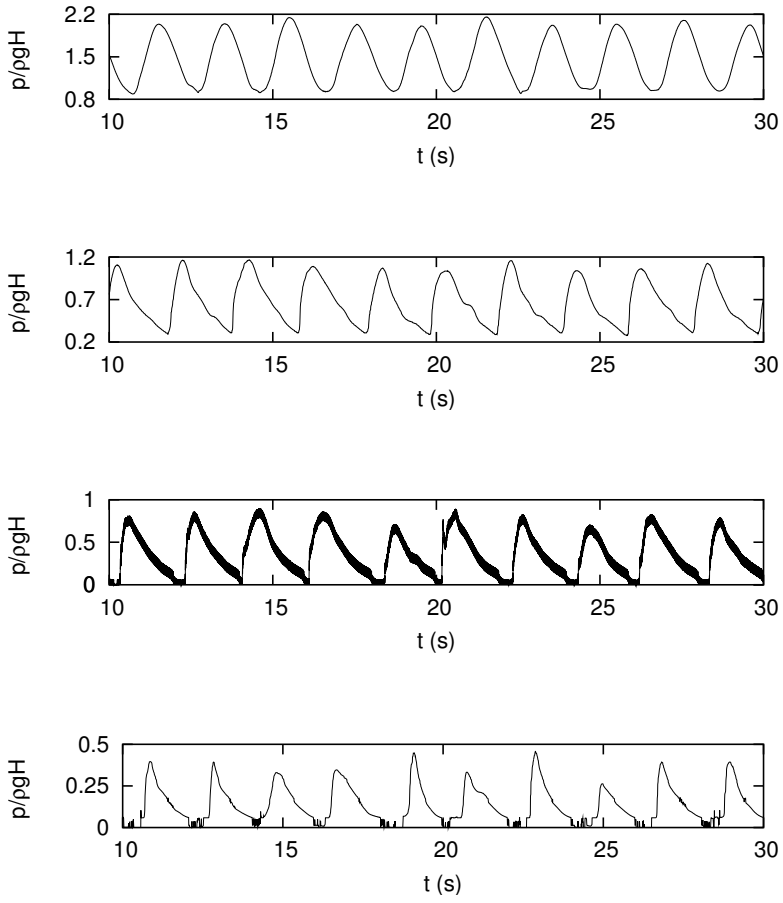

Figure 29: Time signals of the impact pressure on a slope. $PT1$ to $PT4$ represent from top to bottom, respectively.

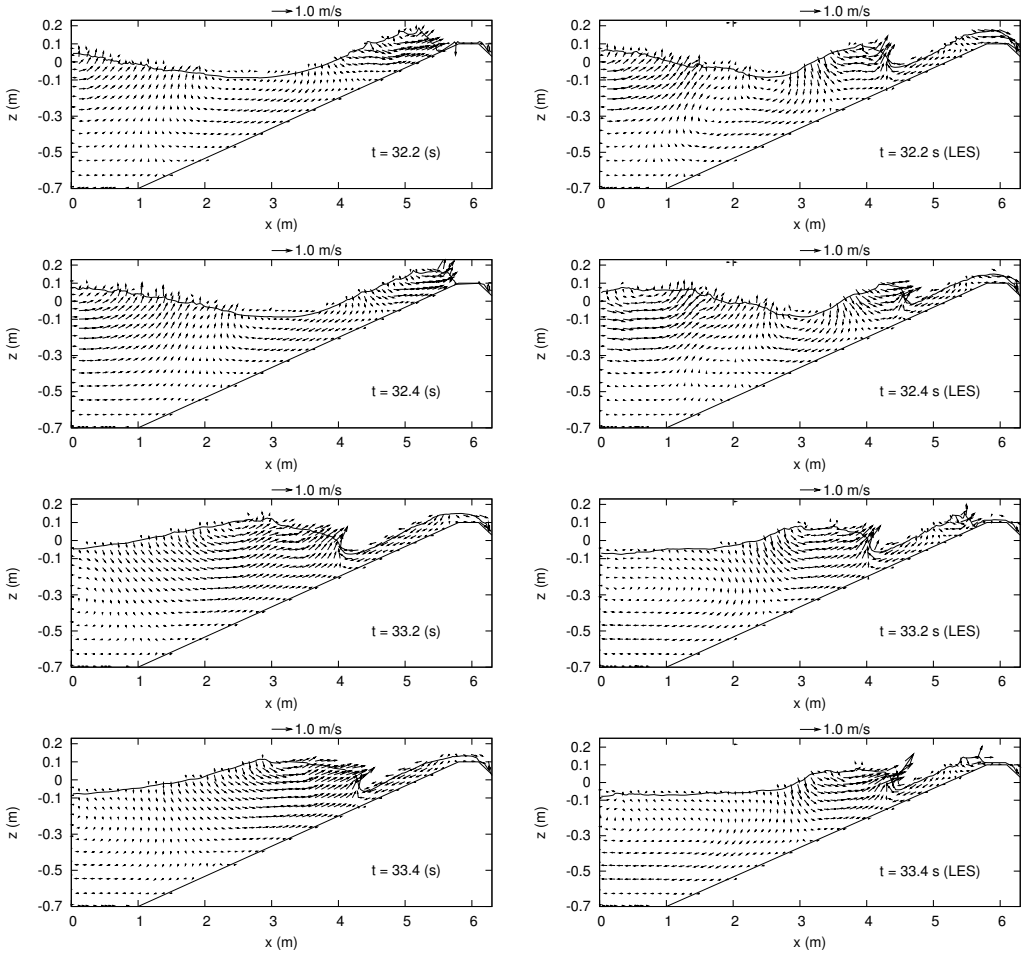

Figure 30: Velocity fields induced by the regular (left) and irregular (right) waves over a sea dike from $t = 32.2$ to 33.4 s.

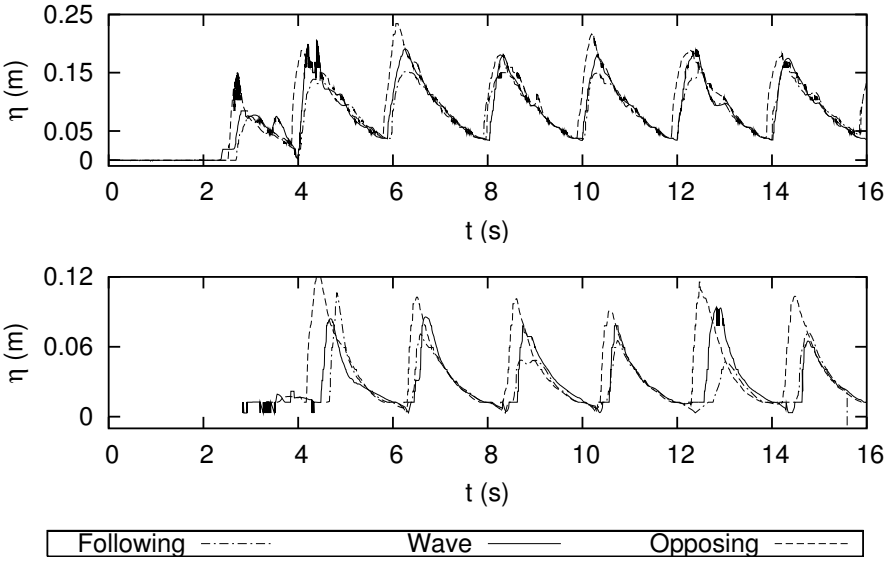

Figure 31: The effects of current at $WG4$ (top) and $WG5$ (bottom) for the surface elevation versus time.

next big wave is approaching the dike. Finally, the wave breaks on the upper reach of the dike at $t = 33.4$ s.

4.6.4 Breaking Wave-Current-Structure Interactions

Fig. 31 shows the effects of two different current speeds (i.e., following- and opposing-current conditions) on waves at two wave gauges of interest: approximately in the surf zone ($WG4$, x=5.2 m from the wave maker), and on the dike crest ($WG5$, x=5.9 m). For the former, a free surface is of very high non-linearity that leads to waves breaking; for the latter, this provides one observation of wave overtopping. By comparison, the change of pure waves at two wave gauges is always between the following- and opposing-currents, as illustrated in Fig. 31. This is a true when one observes the physical model. Additionally, it can be interpreted as the following fact: waves on a positive current are longer than waves on a negative current for given values of T_a and d (see Eq. 39). For the latter, a significant increase in the wave height might take place due to a short wavelength. Actually, the opposite trend may occur, for example, when the waves encounter an ebb flow. Our computations capture this phenomenon. In this case, $|u_c|/u_w$=0.22, indicating that the current strength is not so strong, as expected. Interestingly, waves propagating on a current may experience blocking (the wave energy cannot be transported against the current and finally the waves stop, if the blocking occurs), once the current is sufficiently strong and has a component opposing the waves. Further study, therefore, is necessary to clarify these issues using a numerical modelling. As expected, the effects of current on the wave-induced flows are mainly confined to strongly turbulent regions, as shown in Fig. 32. A high value of the velocity, for example, is subjected to rapid deformation of the free surface at about $x = 4.1$ m in the case of the wave-opposing-current conditions, while a pure wave (in a no-current case) will probably overturn after t=11.2 s but for the following-current case the free surface is not sharp at the corresponding location.

4.6.5 The Effects of Viscosity on the Wave Boundary Layer

Theoretically, the wave boundary layer has to be taken into account, especially when waves break. Instead of $p = 0$ at the free surface (this is defined as the inviscid normal free

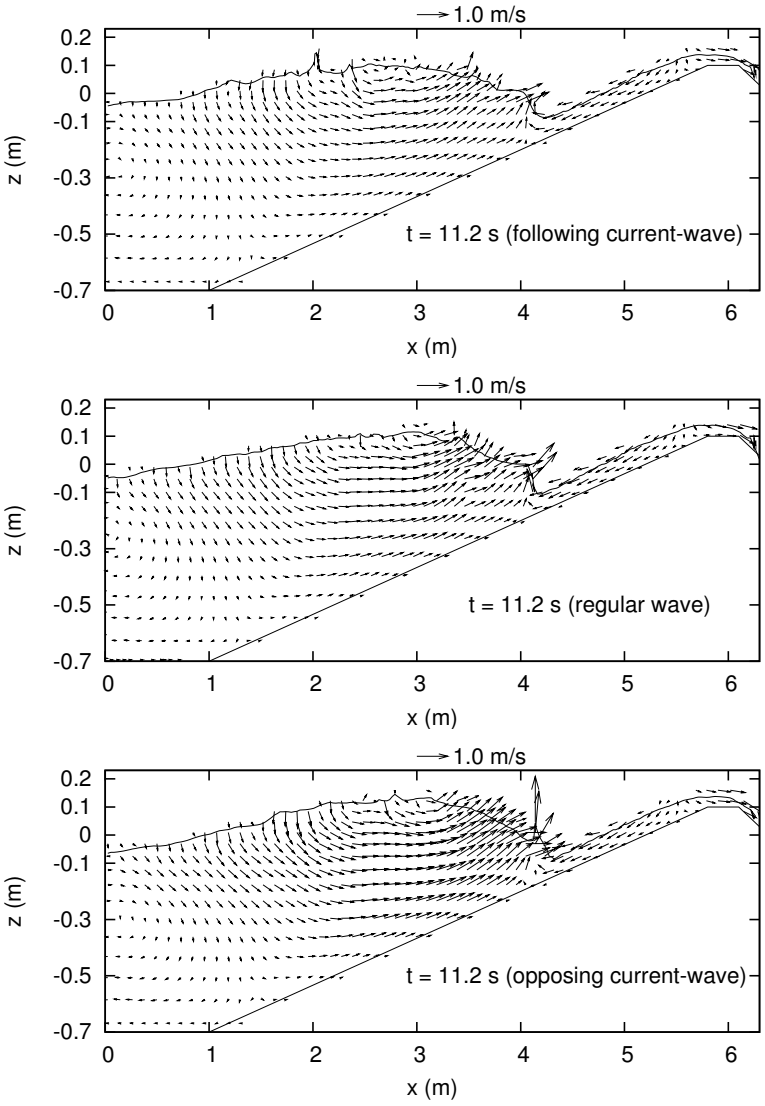

Figure 32: The effects of two different current speeds on the wave-induced velocity fields at one certain time $t = 11.2$.

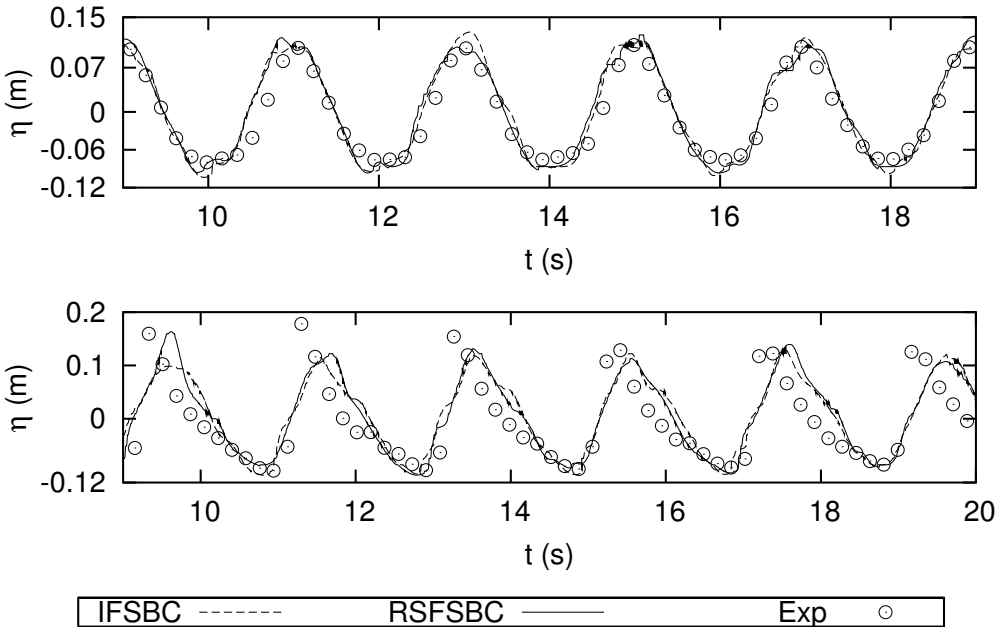

Figure 33: The effects of viscosity on the wave boundary layer at two wave gauges $WG2$ (top) and $WG3$ (bottom), using the RSFSBC.

surface boundary condition (**IFSBC**)), the Reynolds stress free surface boundary condition (**RSFSBC**)[71] is given by

$$p = \rho\left(\nu + \nu_t\right)\left\{2\frac{\partial w}{\partial z} - \frac{\partial h}{\partial x}\left(\frac{\partial u}{\partial z} + \frac{\partial w}{\partial x}\right) - \frac{\partial h}{\partial y}\left(\frac{\partial v}{\partial z} + \frac{\partial w}{\partial y}\right)\right\} \tag{41}$$

indicating that the effects of the subgrid-scale (SGS) models on the free surface can be captured via eddy viscosity ν_t specified by Eq. (40). In this case, the molecular viscosity $\nu = 1.4 \times 10^{-4}\ m^2/s$, and h in Eq. (41) represents the wave height, which can be achieved with the value of $\overline{\alpha}$, according to a VoF approach. Fig. 33 shows the effects of viscosity on the wave boundary layer, when using two types of the free surface dynamic boundary conditions: one is inviscid condition (IFSBC), and the other the Reynolds stress condition (RSFSBC). As can be observed, the RSFSBC can give the accurate prediction, as compared with the IFSBC. The benefits are that its use helps to capture well dynamics within a strong turbulent region, and appreciable errors introduced by approximation of the RSFSBC may be avoided. In particular, the prominent feature of the free surface like the vortex can be generated. To observe the effects of viscosity on the wave motions, on the other hand, we give the flow fields that correspond to the transient flow at one certain time, for example, $t = 17.0$ s, as illustrated in Fig. 34. It is seen that the effects on the solution are certain: this exhibits the strong hydrodynamic phenomena of breakup in the region of high turbulence. A feature is that the shape of the front in this area is changed drastically with the RSFSBC (see Fig. 34).

4.6.6 Three-Dimensional Effects

In the surf zone, flows become highly turbulent when waves break. Based on the fact that turbulence flows are essentially three-dimensional, therefore, a 3D test case is necessary since simulations may depend on the small-scale 3D flows. In this report, the calculated results for 3D case are represented in terms of the wave-induced velocity fields in four cross-sections (see Fig. 35) and the symmetry plane ($y = 0$).

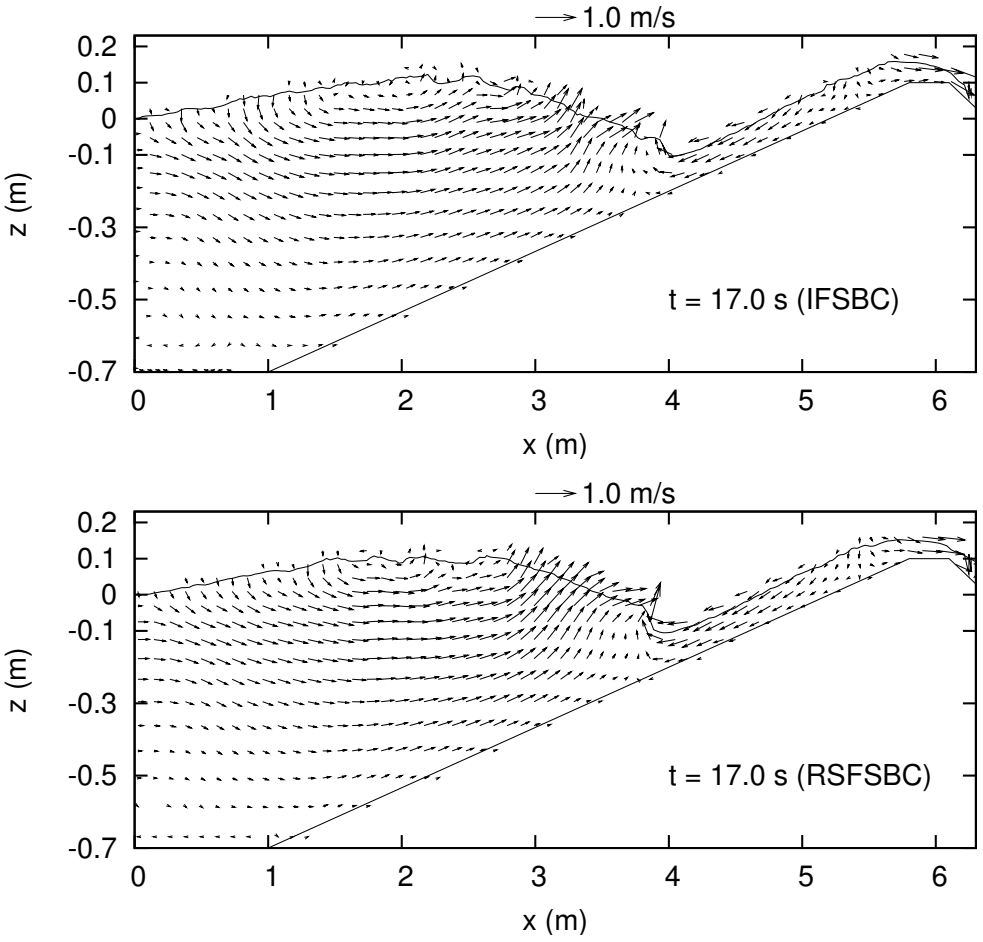

Figure 34: The effects of viscosity on the wave-induced velocity fields at one certain time $t = 17.0$.

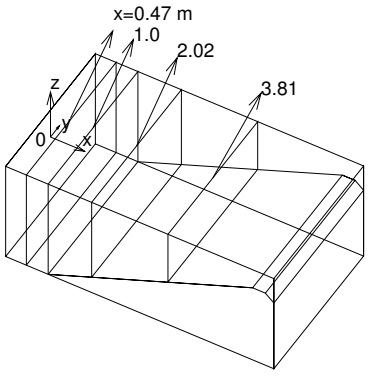

Figure 35: Sketch to illustrate the four cross-sections.

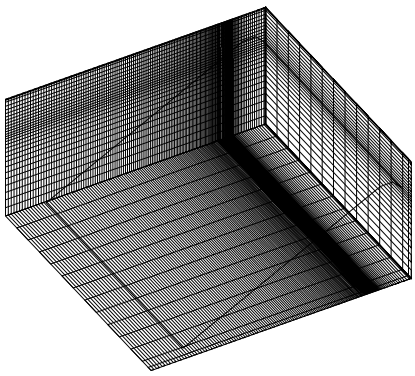

Figure 36: A 3D mesh: $145 \times 15 \times 28$, in the x-, $y-$ and $z-$directions, respectively.

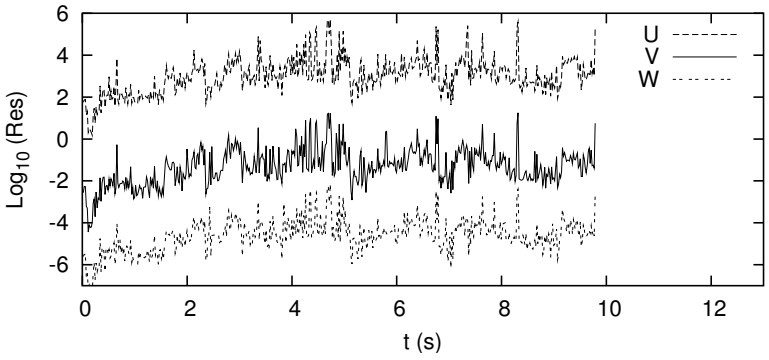

Figure 37: Convergence history for the velocities (U, V, W).

4.6.7 A 3D mesh and convergence history

Fig. 36 shows one 3D Cartesian cut-cell mesh with the number of grid points (60,900). This is one coarse mesh with varying cell sizes in the $x-$ and $z-$directions, respectively, except in the $y-$direction, where the grid spacing is uniform. As expected, the convergence history for residuals of the velocity (U, V, W) almost follows the same trend, as illustrated in Fig. 37. This is because we use a decoupled approach, indicating that the pressure-velocity coupling is not enforced at each iteration. Note that two curves of the residuals for (U, W) are moved up and down in the vertical direction in order to achieve a clear view.

4.6.8 Comparison with measurement

Fig. 38 displays the comparison of the calculated wave height (3D case) with the experimental data available at $WG2$ ($x = 2.02\ m$), including one 2D case. As can be observed, 3D case gives more promising results than 2D case with the grid of 145×28 in the $x-$ and $z-$directions, respectively, as compared with the measurements available. This is our desirable, since the effects of the lateral component (v) of the velocity are considered in the computations, whereas such component tends to be small (see Figs. 39 and 40 for the velocity fields at $t = 1.0$ and 3.5 s). As illustrated in Fig. 39, for example, the flows on the corresponding cross-sections remain axisymmetrical at $t = 1.0$ s, especially with the similar velocity fields ($y = 0$) for both cases at the same time. As time progresses, however, a weak secondary current appears at the plane ($x = 1.0$, located at the toe of the dike) and non-symmetrical shape of the velocity at $x = 3.81$ m (approximately in the surf zone) is

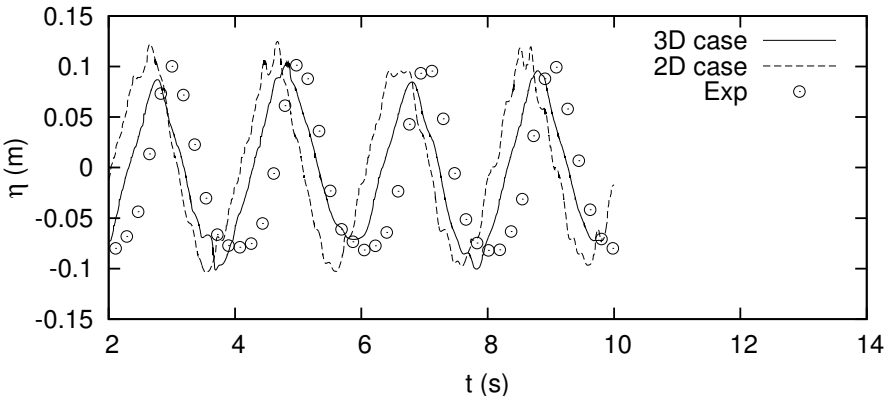

Figure 38: Comparison of the calculated results with experimental data for time history at $WG2$ ($x = 2.02$ m). —— 3D case; − − − 2D case; ◯ Measurement.

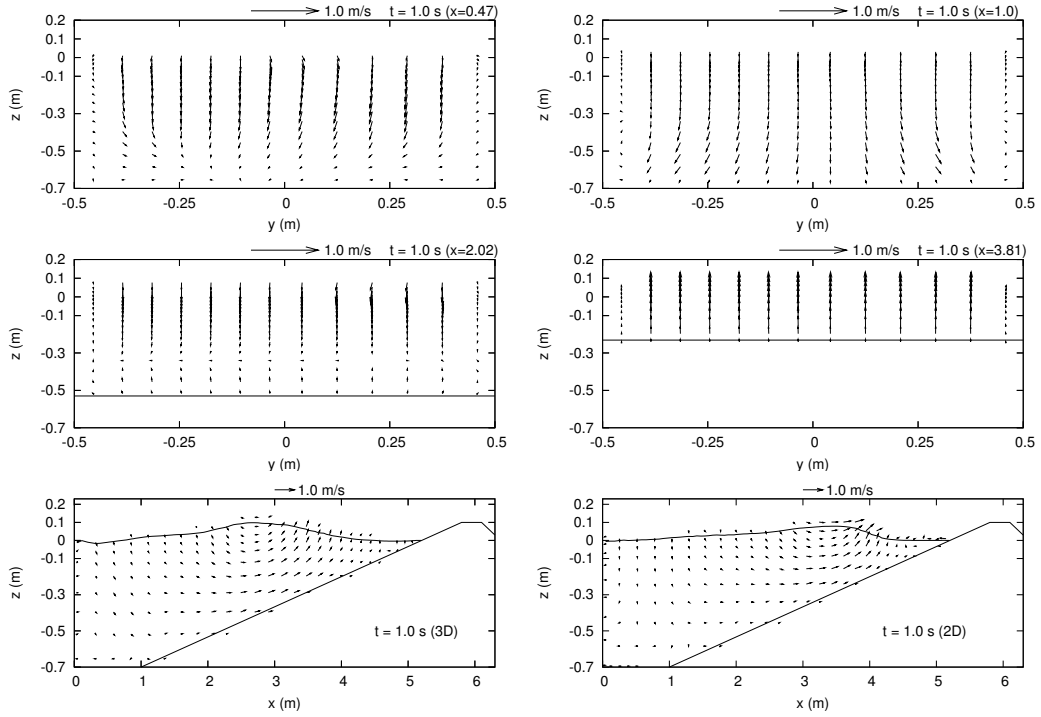

Figure 39: Wave-induced velocity fields at $t = 1.0$ s. Top to middle: $y - z$ plane at $x = 0.47$ to 3.81 m; bottom: symmetry plane, $y = 0$, 3D case (left) and 2D case (right).

captured at $t = 3.5$ s. A significant difference is that overtopping of waves occurs for 2D case but without this one for 3D case, as illustrated in Fig. 40.

To provide a straightforward observation for the wave elevation in the region of interest, on the other hand, we also give a perspective view of the free surface waves (see Fig. 41). This is our preliminary investigation in 3D case for sea dike problems, of course. More testing, for example, with different meshes plus the effects of the domain size, needs to be carried out.

4.7 Conclusions

- Main Points
  - A novel solver available for wave overtopping over sloping and vertical structures;
  - Necessary to consider the effects of surface tension and to use an adequate turbulence model for problems related to the simulation of breaking waves;
  - Simple and effective for our novel VoF solution.
- Ongoing and Future Work:
  - to consider the effects of trapped air pockets;
  - to model wave interaction with porous structures plus development of a local adaptive mesh refinement.

5 Conclusions

The AMAZON-SC code developed by MMU, which provides a numerical wave flume in which the flow equations are solved both in the air and the water, has been extended under the CLASH project to include both the effects viscosity and a porous flow model. The resulting flow code has been applied to examine a selected overtopping event from the experimental study of Samphire Hoe before being applied to examine the effects of scale on the overtopping of a rough, impermeable structure. The scale effects show that that at small scale 1:40 the friction factor is larger than that associated with larger scale tests and that to obtain hydraulic independence tests must be conducted at more than 1:20 scale, assuming that a large armour unit (with a nominal diameter of 4m) is used. For smaller armour units a larger scale will be required to obtain a hydraulically independent Reynolds number.

In Ghent, a new solver based on a Large Eddy Simulation (LES) turbulence model has been developed for the simulation of overtopping of water waves over sloping and vertical structures in a numerical wave tank (NWT). This is a Colume of Fluid (VoF) finite volume solver that incorporates the effects of surface tension. The new solver, which is called **LVOF**, has been verficated and validated with two test cases by

- the consideration of iteration and grid convergence studies;
- and the test using the comparison with measurements available.

for both regular and irregular waves, respectively.

The results demonstrate that UGents new solver can describe most of the significant features of breaking wave-induced flows. In particular, the wave form is well captured even during a lengthy computation, that agrees with measurements available under grid refinements. As a result, this solver can yield detailed information of wave-induced motions on design in coastal engineering using CFD.

The numerical simulations on the Ostia porous breakwater, used for investigating potential scale effects, have been carried out parallel to the numerical development work. In

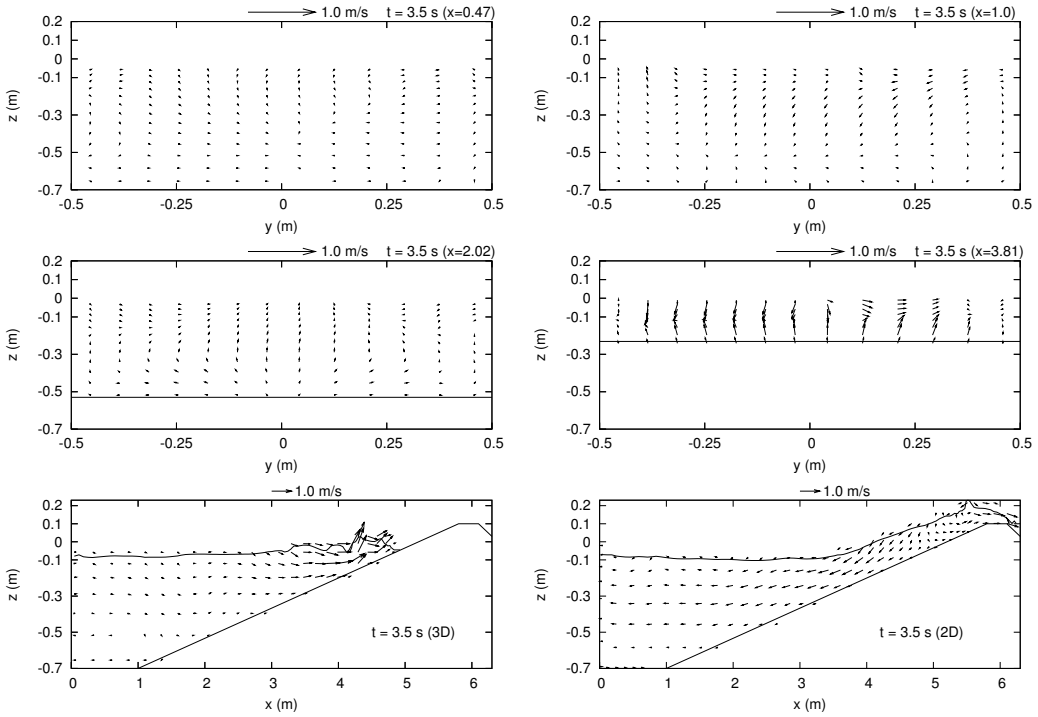

Figure 40: Wave-induced velocity fields at $t = 3.5$ s. Top to middle: $y - z$ plane at $x = 0.47$ to 3.81 m; bottom: symmetry plane, $y = 0$, 3D case (left) and 2D case (right).

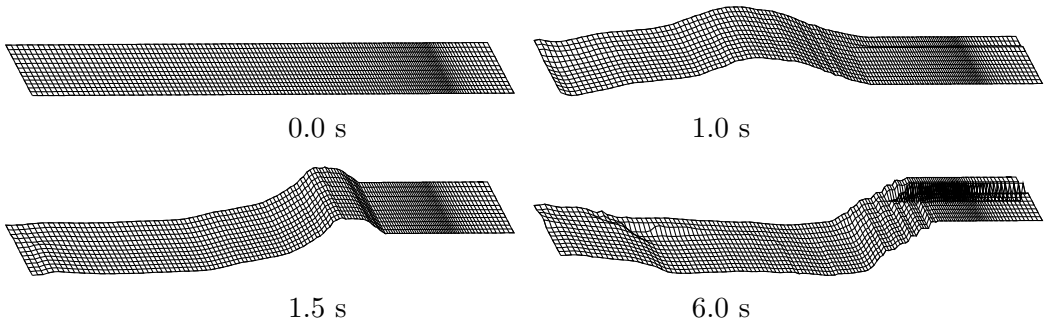

Figure 41: Perspective view of waves.

the report on the numerical work, the progress related to the new numerical code LVOF is presented. As the results from the simulations on the Ostia breakwater are related to the research on scale effects, we suggest that these results and the conclusions will be discussed and reported in relation with Workpackage 7 in the Workpackage 7 report.

References

[1] S Osher and JA Sethian. Fronts propagating with curvature-development speed: Algorithm based on Hamilton-Jacobi formulations. *Jounral of Computational Physics*, 79:12–49, 1998.

[2] M Sussman, P Smereka, and S Osher. A level set approach for computing solutions to incompressible two-phase flow. *Journal of Computational Physics*, 114:146–159, 1994.

[3] JC Park, MH Kim, and H Miyata. Full non-linear free-surface simulations by a 3d viscous numerical wave tank. *International Journal for Numerical Methods in Fluids*, 29(6):658–703, 1999.

[4] SO Unverdi and G Tryggvason. A front-tracking method for viscous, incompressible multifluid flow. *Journal of Computational Physics*, 100:25–37, 1992.

[5] JJ Monaghan. Simulating free surface flows with SPH. *Journal of Computational Physics*, 110:499–406, 1994.

[6] M Sussman and EG Puckett. A coupled level set and volume-of-fluid method for computing 3d and axisymmetric incompressible two-phase flows. *Journal of Computational Physics*, 162:301–337, 2000.

[7] FJ Kelecy and RH Pletcher. The development of a free surface capturing approach for multidimensional free surface flows in closed containers. *Journal of Computational Physics*, 138:939–980, 1997.

[8] J Glimm, J Grove, B Lingquist, OA McBryan, and G Tryggvason. The bifurcation of tracked scalar waves. *SIAM Journal on Scientific and Statistical Computing*, 9(1):61–79, 1988.

[9] J Farm, L Martinelli, and A Jameson. Fast multigrid method for solving incompressible hydrodynamic problems with free surfaces. *AIAA Journal*, 32:1175–1182, 1994.

[10] DL Youngs. Time dependent multi-material flow with large fluid distortion. In KW Morton and MJ Baines, editors, *Numerical Methods for fluid dynamics*, pages 237–285, London, 1982. Academic Press.

[11] CW Hirt and BD Nichols. Volume of Fluid (VoF) methods for dynamics of free boundaries. *Journal of Computational Physics*, 39:201–225, 1981.

[12] B Lafaurie, C Nardone, R Scardovelli, S. Zaleski, and G Zanetti. Modelling merging and fragmentation in multiphase flows with SURFER. *Journal of Computational Physics*, 113:134–147, 1994.

[13] O Ubbink and RI Issa. A method for capturing sharp fluid interfaces on arbitrary meshes. *Journal of Computational Physics*, 153:26–50, 1999.

[14] P Troch, T Li, J De Rouke, and DM Ingram. Wave interaction with a sea dike using a VOF finite-volume method. In JS Chung, M Prevosto, N Mizutani, GH Kim, and ST Grilli, editors, *Proceedings of the 13th International Offshore and Polar Engineering Conference*, volume 3, pages 325–332. International Society of Offshore and Polar Engineering, 2003.

[15] WJ Rider and DB Kothe. Reconstructing volume tracking. *Journal of Computational Physics*, 141:112–152, 1998.

[16] HS Udaykumar, R Mittal, and W Shyy. Computation of solid-liquid phase fronts in the sharp interface limit on fixed grids. *Journal of Computational Physics*, 153:535–574, 1999.

[17] O Ubbink. *Numerical prediction of two fluid systems with sharp interface*. PhD thesis, Imperial College, London, 1997.

[18] T Li, P Troch, and J De Rouck. A solver for numerical simulation of breaking waves using a cut-cell vof cell-staggered finite-volume approach. Technical report, Department of Civil Engineering, Ghent University, Belgium, 2003.

[19] T Li, P Troch, and J De Rouck. Wave overtopping over a sea dike. *Journal of Computational Physics*, 198:686–726, 2004.

[20] T Li, P Troch, and J De Rouck. Large eddy simulation of wave overtopping on nonuniform cartesian cut-cell grids. In JS Chung, K Izumiyama, M Sayed, and SW Hong, editors, *Proceedings of The Fourteenth (2004) International Offshore and Polar Engineering Conference, Toulon, France*, volume 3, pages 276–284. ISOPE, Cupertino, California, USA, 2004.

[21] JF Thompson, ZAU Warsi, and C Wayne-Mastin. *Numerical Grid Generation: Foundation and Applications*. Elsevier Science Publishing, 1985.

[22] NP Weatherill and CR Forsey. Grid Generation and Flow Calculations for Complex Aircraft Geometries Using a Multi-Block Scheme. *AIAA paper 84-1665*, 1984.

[23] JL Steger, FC Dougherty, and JA Benek. A Chimera Grid Scheme. In *Advances in Grid Generation, ASME FED-5*, pages 59–69, 1983.

[24] C. M. Albone. Embedded Meshes of controllable Quality Synthesised from Elementary Geometric Features. paper 92-0662, AIAA, 1992.

[25] J Rantakokko. Partitioning strategies for structured multiblock grids. *Parallel Computing*, 26(12):1661–1680, 2000.

[26] J. Peraire, M. Vahdati, K. Morgan, and O. C. Zienkiewicz. Adaptive Remeshing for Compressible Flow Computations. *Journal Comp. Physics*, 72:449–466, 1987.

[27] D De Zeeuw and KG Powell. An Adaptively Refined Cartesian Mesh Solver for the Euler Equations. *Journal of Computational Physics*, 104(1):56–68, 1993.

[28] R Löhner. A parallel advancing front grid generation scheme. *International Journal for Numerical Methods in Engineering*, 51(6):663–678, 2001.

[29] M Delanaye, A Patel, B Leonard, and C Hirsch. Automatic unstructured hexahedral grid generation and flow solutions. In *ECCOMAS CFD 2001*. IMA, Southend-on-sea, UK, 2001.

[30] MJ Berger and RJ LeVeque. An Adaptive Cartesian Mesh Algorithm for the Euler Equations in Arbitrary Geometries. *AIAA Paper 89-1930-CP*, 1989.

[31] JJ Quirk. An Alternative to Unstructured Grids for Computing Gas Dynamic Flows Around Arbitrarily Complex Two-Dimensional Bodies. *Computers & Fluids*, 23(1):125–142, 1994.

[32] G Yang, DM Causon, DM Ingram, R Saunders, and P Batten. A Cartesian Cut Cell Method for Compressible Flows - Part A : Static Body Problems. *Aeronautical Journal*, 101(1001):47–56, 1997.

[33] G Yang, DM Causon, and DM Ingram. Calculation of compressible flows about complex moving geometries using a 3d Cartesian cut cell method. *International Journal for Numerical Methods in Fluids*, 33:1121–1151, 2000.

[34] S Cieslak, S Ben Khelil, I Choqiet, and A Merlen. Cut cell stategy for 3d blast wave numerical simulation. *Shock Waves*, 10(6):421–429, 2001.

[35] DM Causon, DM Ingram, CG Mingham, G Yang, and RV Pearson. Calculation of shallow water flows using a cartesian cut cell approach. *Advances in Water Resources*, 23:545–562, 2000.

[36] L Qian, DM Causon, DM Ingram, and CG Mingham. A cartesian cut cell method for incompressible viscous flows. In *ECCOMAS CFD 2001*. IMA, Southend-on-Sea, UK, 2001.

[37] PG Tucker and Z Pan. A cartesian cut cell method for incompressible viscous flow. *Applied Mathematical Modelling*, 24:591–606, 2000.

[38] T Ye, R Mittal, HS Udaykumar, and W Shyy. An accurate cartesian grid method for viscous incompressible flows with complex immersed boundaries. *Journal of Computational Physics*, 156:209–240, 1999.

[39] RJ LeVeque and KM Shyue. Two dimensional front tracking based on high resolution wave propagation methods. *Journal of Computational Physics*, 123:354–368, 1996.

[40] HS Udaykumar, HC Kan, W Shyy, and R Tran-Son-Tay. Multiphase dynamics in arbritary geometries on fixed cartesian grids. *Journal of Computational Physics*, 137:366–405, 1997.

[41] MJ Ivings. *Wave Propagation through Gases and Liquids*. PhD thesis, Department of Computing and Mathematics, Manchester Metropolitan University, 1997.

[42] F Stern, V Wilson, HW Coleman, and EG Paterson. Verification and validation of cfd simulations. Technical Report 407, IIHR Report, 1999.

[43] L Qian, DM Causon, DM Ingram, and CG Mingham. A two-fluid solver for hydraulic applications. In WR Blain and CA Brebbia, editors, *Hydraulic Information Management*, number 10 in Water Studies Series, pages 327–336. WIT Press, 2002.

[44] L Qian, DM Causon, DM Ingram, and CG Mingham. A cartesian cut cell two-fluid solver for hydraulic flow problems. *ASCE Journal of hydraulic Engineering*, 129(9):688–696, 2003.

[45] DM Causon, DM Ingram, CG Mingham, and RV Pearson. A cartesian cut cell method for shallow water flows with moving boundaries. *Advances in Water Resources*, 24(2001):899–911, 2001.

[46] B van Leer. On the Relation Between the Upwind-Differencing Schemes of Godunov, Engquist-Osher and Roe. *SIAM Journal on Scientific and Statistical Computing*, 5(1):1–20, 1984.

[47] AK Runchal. Condif: A modified central-difference scheme for convective flows. *International Journal for Numerical Methods in Engineering*, 24:1593–1608, 1987.

[48] DK Clarke, MD Salas, and HA Hassan. Euler Calculations for Multielement Airfoils Using Cartesian Grids. *AIAA Journal*, 24(3):353–358, 1986.

[49] Y. Chiang, B. Van Leer, and K. G. Powell. Simulation of Unsteady Inviscid Flow on an Adaptively Refined Cartesian Grid. *AIAA Paper 92-0443*, 1992.

[50] DM Ingram, DM Causon, and CG Mingham. Developments in Cartesian cut cell methods. *Mathematics and Computers in Simulation*, 61:561–572, 2003.

[51] A Chorin. The numerical solution of the Navier-Stokes equations for an incompressible fluid. Report NYO-1480-82, New York University, 1967.

[52] WY Soh and JW Doodrich. Unsteady solution of incompressible Navier-Stokes equations. *Journal of Computational Physics*, 79:113–134, 1988.

[53] SE Rogers and D Kwak. An upwind difference scheme for the time-accurate incompressible Navier-Stokes equations. *AIAA Journal*, pages 113–134, 1990.

[54] M Beddhu, LK Taylor, and DL Whitfield. A time accurate calculation procedure for flows with a free surface using a modified artificial compressibility formulation. *Applied Mathematics and Computation*, 65(1):33–48, 1994.

[55] D Pan and H Lomax. A new approximate LU factorisation scheme for the Navier-Stokes equations. *AIAA Journal*, 26:163–171, 1988.

[56] L Qian, DM Causon, DM Ingram, and CG Mingham. A pressure splitting scheme for free-surface capturing methods for flows with gravity effects. *Journal of Computational Physics*, page submitted, 2003.

[57] CJ Huang, HH Chang, and HH Hwung. Structural permeability effects on the interaction of a solitary wave and a submerged breakwater. *Coastal Engineering*, 49(2003):1–24, 2003.

[58] AM Arbhabhiramar and AA Dinoy. Friction factor and reynolds number in porous media flow. *Journal of the Hydraulics Division, ASCE*, 99(HY6):901–911, 1973.

[59] WS Fu, HC Huang, and WY Liou. Thermal enhancement in laminar channel flow with a porous block. *International Journal of Heat and Mass Transfer*, 39(10):2165–2175, 1996.

[60] T Pullen, NWH Allsop, T Bruce, J Pearson, and J Geeraerts. Violent wave overtopping at Samphire Hoe: field and laboratory measurements. In *Proceedings of the 29th International Congress on Coastal Engineering*, page Paper No. 316, 2004.

[61] KP Schulz. Maßstabseffekte beim wellenauflauf auf glatten und rauhen böschungen (scale effects on smooth and rough slopes). Technical Report Heft 120, pp 135–244, Mitteilungen Leichtweiß-Institut für Wasserbau der Technischen Universität Braunschweig, 1992.

[62] T Sakakiyama and R Kajima. Scale effects on wave overtopping of seawall covered with armour units. In *Proceedings 26th International Conference Coastal Engineering (ICCE)*, 1998.

[63] R Kajima and T Sakakiyama. Review of works using CRIEPI flume and present work. In AS Arcilla, MJF Stive, and NC Kraus, editors, *Coastal Dynamics '94 - Proceedings of an International Conference on the Role of the Large Scale Experiments in Coastal Research*, pages 614–627. ASCE, New York, 1994.

[64] EG Puckeet, AS Almgren, JB Bell, DL Marcus, and WJ Ride. A high-order projection method for tracking fluid interface in variable density incompressible flows. *Jounral of Computational Physics*, 130:269–282, 1997.

[65] D Gueyffier, J Li, A Nadim, R Scardovelli, and S Zaleski. Volume-of-fluid interface tracking with smoothed surfaces stress methods for three-dimensional flows. *Journal of Computational Physics*, 152:423–456, 1999.

[66] DJE Harvie and DF Fletcher. A new volume of fluid algorithm: the defined donating region scheme. *International Journal for Numerical Methods in Fluids*, 35(2):151–172, 2001.

[67] M Rudman. Volume-tracking methods for interfacial flow calculations. *International Journal for Numerical Methods in Fluids*, 24(7):671–691, 1997.

[68] F Xiao. A computational model for suspended large rigid bodies in 3d unsteady viscous flows. *Journal of Computational Physics*, 155:348–379, 1999.

[69] JU Brackbill, DB Kothe, and C Zemach. A continuum method for modelling surface tension. *Jounral of Computational Physics*, 100:335–354, 1992.

[70] B van Leer. Towards the Ultimate Conservative Difference Scheme IV. A New Approach to Numerical Convection. *Journal of Computational Physics*, 23:276–299, 1977.

[71] T Li. Computation of turbulent free-surface flows around modern ships. *International Journal for Numerical Methods in Fluids*, 43(4):407–430, 2003.

[72] DS Kershaw. The incomplete cholesky-conjugate gradient method for the iterative solution of system of linear equation. *Journal of Computational Physics*, 26:43–65, 1978.